A Two-Phase SPH Model for Massive Sediment Motion in Free Surface Flows

Huabin Shi[1], Pengfei Si[2], Ping Dong[3], Xiping Yu[4]

Abstract

Massive sediment motion in water with a free surface is an important kind of geophysical flows such as hyper-concentrated sediment laden river flows discharging into estuarine delta and turbidity currents generated by subaqueous landslides. One of the key and common characteristics of such flows is that interactions between water and sediment as well as those among sediment particles are equally important in affecting the sediment motion and the fluid flow. This paper presents a numerical model that builds on and extends an earlier two-phase SPH model based on a continuum ~~description~~ formulation of solid-liquid mixtures [Comput. Phys. Commun. 221 (2017) 259] to provide a unified description of ~~account for~~ massive sediment motion in free surface flows. In the model, a constitutive law based on the rheology of dense granular flow is introduced to express the intergranular stresses while the interphase drag force is determined by combining the Ergun equation for dense solid-fluid mixtures and the power law for dilute suspensions. ~~The model can thus represent not only sediment transport by water flows but also gravity-induced underwater granular flows.~~ The proposed model is firstly applied to the study of collapse of loosely or densely packed granular columns

[1] Research Associate, School of Engineering, University of Liverpool, Liverpool, United Kingdom. Email: huabin.shi@liverpool.ac.uk

[2] Ph.D. Candidate, State Key Laboratory of Hydroscience and Engineering, Department of Hydraulic Engineering, Tsinghua University, Beijing, China. Email: spf14@mails.tsinghua.edu.cn

[3] Professor, School of Engineering, University of Liverpool, Liverpool, United Kingdom. Email: ping.dong@liverpool.ac.uk

[4] Corresponding author, Professor, State Key Laboratory of Hydroscience and Engineering, Department of Hydraulic Engineering, Tsinghua University, Beijing, China. Email: yuxiping@tsinghua.edu.cn

submerged in water. The computed surface profiles of the granular column are found to be in good agreement with the experimental data. It shows that the loosely packed and the densely packed columns behave rather differently due to the differences in water-sediment interaction processes. The model is then used to simulate a dam-break flow over a mobile sediment bed. The computed configurations of the flow and the movable bed also agree well with the measured data. The predicted position on the leading edge of the flow has a mean error of 0.8% while the mean error for the maximum bed height is 12.9%. To further identify the dynamic processes involved, effects of water-sediment interactions on the motion of bed materials are investigated by examining the spatial and temporal variations of pressure and flow velocity. As shown in the applications, the proposed two-phase SPH model can successfully represent both the gravity-driven underwater granular flows and the shear flow driven intense sediment transport, implying its potential use in practical scenarios in which the two kinds of flows exist simultaneously, such as landslides triggered by storm in shallow sea and flows resulted in barrier or dam breaks.

Keywords: Two-phase SPH model; Sediment motion; Water-sediment interactions; Underwater granular column collapse; Dam-break erosion

1 Introduction

Massive sediment motion in free surface flows often occurs in nature. One example is the large-scale submarine landslide which has been reported to be the main cause of several destructive tsunamis (Keating and McGuire, 2000; Lynett and Liu, 2002). The rapid erosion of riverbed by dam-break flow, which may result in significant morphological changes of the channel system and increased flooding risk, is another typical case (Capart and Young, 1998; Wu and Wang, 2007). Consequently, accurate prediction of massive sediment motion in free surface flows is essential in disaster prevention and mitigation as well as in infrastructure safety assessment.

Massive sediment motion in free surface flows, including the gravity-induced underwater granular flow and the shear flow driven intense sediment transport, is characterized by the high concentration of the particle phase. Although the flows may be different in driving forces, the stresses generated by interphase and intergranular interactions within the solid-liquid mixtures are intrinsically the same and play a similarly important role in the flows ~~Both interphase forces and intergranular stresses are thus important~~ (Dong and Zhang, 2002; Shi and Yu, 2015; Lee and Huang, 2018). In some situations, the large deformation of free water surface may also occur (Spinewine, 2005). Therefore, a unified numerical model for different types of massive sediment motion is required to accurately describe the interactions not only between water and sediment but also among sediment particles at a wide range of sediment concentration and to be capable of capturing the complex deformation of the free water surface.

This is however not an easy task. As most of the available numerical models for sediment motion adopt mesh-based Eulerian approach, they have difficulties in simulating the complicated deformation and fragmentation of free water surface (Fu and Jin, 2016). At a more fundamental level, it requires improved understanding and formulations of intergranular stresses and interphase forces (Bakhtyar et al., 2010; Chauchat, 2018) with a two-phase model in which the primary flow variables of both water and sediment are fully resolved (Dong and Zhang, 1999; Bakhtyar et al., 2010).

Mesh-free particle methods, such as the Smoothed Particle Hydrodynamics (SPH) and the Moving Particle Semi-implicit (MPS) methods, have proven to be powerful in tracking the violent motion of free water surface (Gotoh and Khayyer, 2018), and have also been introduced to the simulation of sediment laden flows (Ulrich et al., 2013; Fourtakas and Rogers, 2016; Nodoushan et al., 2018). However, most of the existing particle models for sediment motion are not formulated strictly in the two-phase framework. Instead, they treat clear water and sediment-water mixture as two immiscible fluids and represent the two phases by different sets of SPH/MPS particles. The sediment phase considered in these models is a mixture of water and sediment, and variables of the mixture rather than those of each individual phase are solved. As a result, they are unable to address directly the intergranular stresses and the interphase forces. Furthermore, suspended load cannot be rigorously resolved by these two-immiscible-fluid models and it was just approximated by a kernel-averaged volumetric sediment concentration (Ulrich et al., 2013; Zubeldia et al., 2018). Only a few attempts (Bui et al., 2007; Wang et al., 2016; Pahar and Dhar, 2017; Shi et al., 2017) have been made to develop a complete two-phase particle method for liquid-solid mixtures, all of which, however, contain some questionable assumptions. For instance, the variation of sediment concentration was ignored in Pahar and Dhar (2017); idealized constitutive laws for intergranular stresses, i.e., the elastic-perfect plastic model was assumed in Bui et al. (2007). Shi et al. (2017) recently presented a two-phase SPH model for suspended sediment motion in free surface flows, which performed well both in idealized and in practical problems with suspended load. However, the formulations for intergranular stresses and interphase drag force in the model are not sufficiently accurate under high-concentration conditions.

In this paper, the two-phase SPH model developed by the authors (Shi et al., 2017), which is formulated strictly in a two-phase framework, ~~Shi et al. (2017)~~ is extended to describe massive sediment motion. It is aimed to give a unified description of gravity-induced underwater granular flows and intense sediment transport by flowing water. ~~represent not only sediment transport by water flows but also gravity-induced underwater granular flows.~~ The structure of the model remains unchanged, but a number of substantial improvements have been introduced to better describe the underlying physics of dense sediment motion. Specifically, a constitutive law based on the rheology of dense granular flows is used to represent the intergranular stresses. To estimate the interphase drag force in both high- and low-concentration regimes, the Gidaspow (1994) formula is adopted, which combines the Ergun equation for dense solid-fluid mixtures and the power law for dilute suspensions. The proposed model is applied to the study of collapse of underwater granular columns and bed erosion by dam-break flows. In the former case, the flow is driven by the falling of sediments into still water, while in the latter the falling water causes rapid erosion of the mobile sediment bed and strong near-bed sediment suspension. The computed surface profiles of both loosely and densely packed granular columns submerged in still water with a free surface are compared with experimental data. Effects of water-sediment interactions on the collapse of loosely/densely packed columns are examined. The fluid flow within the granular material is simulated and the evolution of water vortex in the process of granular column collapse is discussed. For the dam-break induced erosion problem, the computed configurations of the free water surface and the movable bed are compared with experimental results. The effects of water-sediment interactions on both the motion of bed materials and the bed erosion process are investigated.

The rest of the paper is organized as follows. The governing equations of the two-phase model and their SPH formulations are described in Section 2. Applications of the model to underwater granular column collapse and sediment transport by dam-break flow are presented in Sections 3 and 4, respectively. Finally, conclusions are drawn in Section 5.

2 A two-phase SPH model for intense sediment transport

2.1 Governing equations for the two phases

The continuum description of a sediment-water mixture flow is based on the assumption that water and sediment are coupled two phases within the domain of interest. Both phases are governed by the conservation laws for mass and momentum. The general two-fluid form of continuity and momentum equations for two-phase flows originally derived by Drew (1983) are employed in this study. To deal with the turbulence of the two phases, the sub-particle scaling technique (Dalrymple and Rogers, 2006; Mayrhofer et al., 2015) is applied. The governing conservation equations are then spatially filtered by virtue of the Favre averaging (Shi et al., 2017). The filtered continuity equations are

$$\frac{\partial\left(\alpha_f \rho_f\right)}{\partial t}+\frac{\partial\left(\alpha_f \rho_f u_{f,j}\right)}{\partial x_j}=0 \tag{1}$$

$$\frac{\partial\left(\alpha_s \rho_s\right)}{\partial t}+\frac{\partial\left(\alpha_s \rho_s u_{s,j}\right)}{\partial x_j}=0 \tag{2}$$

in which, t is the time; x is the coordinate, and $i, j=1, 2, 3$ represent the coordinate directions, for which the summation convention is valid; the subscripts f and s represent the water phase and the sediment phase, respectively; α is the volume fraction, and $\alpha_f+\alpha_s=1$; ρ is the density; u is the velocity.

The filtered momentum equations for the two phases are written as

$$\frac{\partial\left(\alpha_f\rho_f u_{f,i}\right)}{\partial t}+\frac{\partial\left(\alpha_f\rho_f u_{f,i}u_{f,j}\right)}{\partial x_j}=-\alpha_f\frac{\partial p_f}{\partial x_i}+\frac{\partial\left[\alpha_f\left(\tau^0_{f,ij}+\tau^t_{f,ij}\right)\right]}{\partial x_j}+\alpha_f\rho_f g_i-F_i \tag{3}$$

$$\frac{\partial\left(\alpha_s\rho_s u_{s,i}\right)}{\partial t}+\frac{\partial\left(\alpha_s\rho_s u_{s,i}u_{s,j}\right)}{\partial x_j}=-\alpha_s\frac{\partial p_f}{\partial x_i}+\frac{\partial\left[\alpha_s\left(\tau^0_{s,ij}+\tau^t_{s,ij}\right)\right]}{\partial x_j}+\alpha_s\rho_s g_i+F_i \tag{4}$$

where, p is the pressure; τ^0_f is the viscous stress of the water phase, while τ^0_s is the intergranular stress of the sediment phase; τ^t is the sub-particle scale (SPS) stress; g is the gravitational acceleration; F is the force on the solid phase by water excluding the pressure-gradient-related buoyancy, which is a part of the first terms on the right side of the momentum equations. F is formulated in the subsection on two-phase interactions.

The viscous stress $\boldsymbol{\tau}^0_f$ and the intergranular stress $\boldsymbol{\tau}^0_s$ are determined by

$$\tau^0_{f,ij}=\rho_f\nu^0_f\left(2S_{f,ij}-\frac{2}{3}S_{f,ll}\delta_{ij}\right) \tag{5}$$

$$\tau^0_{s,ij}=\rho_s\nu^0_s\left(2S_{s,ij}-\frac{2}{3}S_{s,ll}\delta_{ij}\right)-p_s\delta_{ij} \tag{6}$$

$$S_{k,ij}=\frac{1}{2}\left(\frac{\partial u_{k,i}}{\partial x_j}+\frac{\partial u_{k,j}}{\partial x_i}\right) \tag{7}$$

in which, $k=f,s$; $S_{k,ij}$ are the rate-of-strain tensors of the two phases; ν^0_f and ν^0_s are the kinematic viscosities; p_s is the intergranular pressure of the sediment phase, resulting from enduring contact, collision, and friction between the solid particles. The viscosity ν^0_s and the pressure p_s are estimated by a rheology-based constitutive law for the sediment phase in the following subsection.

The SPS stresses $\boldsymbol{\tau}^t_k$ are modelled based on Boussinesq hypothesis:

$$\tau^t_{k,ij}=\rho_k\nu^t_k\left(2S_{k,ij}-\frac{2}{3}S_{k,ll}\delta_{ij}\right) \tag{8}$$

where, ν^t_k ($k=f,s$) are the eddy viscosities of the two phases. The well-known Smagorinsky model (Smagorinsky, 1963) is utilized to determine ν^t_k, but a modification is made to consider the turbulence damping by sediment particles (Chen et al., 2011):

$$\nu_k^t = \left(C_k \Delta\right)^2 \left|\mathbf{S}_k\right| \left(1 - \frac{\alpha_s}{\alpha_{sm}}\right)^n \tag{9}$$

in which, Δ is the characteristic length of filter, which is set to be the initial particle size in a SPH model; $\mathbf{S}$ is the rate-of-strain tensor, and its norm $\left|\mathbf{S}_k\right| = \sqrt{2S_{k,ij}S_{k,ij}}$; α_{sm} is the maximum sediment volumetric concentration, at which the turbulence is assumed to be totally suppressed; n is a coefficient; C is Smagorinsky constant. In this study, α_{sm} is set to be equal to the jamming volume fraction defined in the following subsection, at which the dense sediment phase is in static. As in Shi et al. (2017), $n = 5$ and $C_f = C_s = 0.1$.

In the present study, the weakly compressible SPH (WCSPH) approach is adopted. Specifically, the water phase is assumed to be weakly compressible, and the water density ρ_f is thus a variable. The equation of state (EOS) proposed by Shi et al. (2017) is utilized to compute the fluid pressure p_f in the sediment-water mixture:

$$p_f = \frac{\rho_{f0} c_0^2}{\xi} \frac{\alpha_f \rho_f + \alpha_s \rho_{f0}}{\alpha_f \rho_f} \left[\left(\frac{\alpha_f \rho_f + \alpha_s \rho_{f0}}{\rho_{f0}} \right)^{\xi} - 1 \right] \tag{10}$$

where, $\xi = 7$; $\rho_{f0} = 1000\ \mathrm{kg \cdot m^{-3}}$ is the reference water density at $p_f = 0$; c_0 is the sound speed in water at the reference density, which is usually set to be ten times the maximum water velocity in the problem of interest.

2.2 A rheology-based constitutive law for intergranular stresses

A constitutive law based on the rheology of dense granular flows (Lee et al., 2016; Chauchat, 2018) is employed to represent the intergranular stresses of the particles phase in sediment-water mixture flows. This law depends on the frictional characteristic of granular materials, i.e., the shear stress components are related to the pressure. It has been successfully applied to bedload transport (Chiodi et al., 2014), sheet flows (Lee et al., 2016), and underwater granular column collapse (Lee and Huang, 2018).

In the constitutive law, the sediment pressure p_s has two components, a shear-rate-dependent component p_s^r for the rheological characteristics of the bulk granular materials and a shear-rate-independent component p_s^e for the enduring elastic contact between the solid particles:

$$p_s = p_s^r + p_s^e \tag{11}$$

Boyer et al. (2011) and Trulsson et al. (2012) carefully investigated the rheological characteristics of the dense granular materials in an interstitial fluid. It is found that the rheology of dense granular materials is dominated by both inter-particle forces and viscosity of the interstitial fluid. According to their results, the shear-rate-dependent component p_s^r can be evaluated by

$$p_s^r = \left(\frac{c_1\alpha_s}{\alpha_{s0}-\alpha_s}\right)^2 \left(\rho_f \nu_f^0 + c_2\rho_s d_s^2 |\mathbf{S}_s|\right)|\mathbf{S}_s| \tag{12}$$

where, α_{s0} is the jamming volume fraction, which is the maximum packing fraction of the sheared granular particles; d_s is the diameter of sediment particles; c_1 and c_2 are model parameters. On the other hand, when the packing fraction α_s increases to the random loose-packing concentration α_*, the component p_s^e comes into play. As the volume fraction increases further to the random close-packing concentration α^*, the granular materials present a transition from fluid-like to solid-like behavior (Johnson and Jackson, 1987). Following Hsu et al. (2004) and Lee et al. (2016), the shear-rate-independent pressure p_s^e is estimated by

$$p_s^e = \begin{cases} 0 & \alpha_s < \alpha_* \\ K\left(\alpha_s-\alpha_*\right)^\chi \left[1+\sin\left(\pi\dfrac{\alpha_s-\alpha_*}{\alpha^*-\alpha_*}-\dfrac{\pi}{2}\right)\right] & \alpha_s \ge \alpha_* \end{cases} \tag{13}$$

in which, K is a coefficient related to the Young's modulus and the Poisson's ratio of the solid material; χ is a model parameter. Generally, the parameters $c_1 = 0.75 \sim 1.00$, $c_2 = 0.01 \sim 1.00$, and $\chi = 1.5 \sim 5.5$ (Trulsson et al., 2012; Chiodi et al., 2014; Lee and Huang, 2018; Chauchat, 2018), and in the present computations their values as well as that of K are determined based on sensitivity studies. In the applications, values of α_{s0}, α_*, and α^* are set depending on the specific solid materials.

Relating the viscous stress of sediment phase to the inter-granular pressure according to the frictional law and introducing the Papanastasiou regularization technique (Papanastasiou,

1987) to avoid singularity in the expression for viscosity, we obtain

$$\nu_s^0 = \frac{\mu p_s}{\rho_s \left|\mathbf{S}_s\right|}\left(1 - e^{-m\left|\mathbf{S}_s\right|}\right) \tag{14}$$

where, μ is the friction coefficient of the assembly of sediment particles, varying with the inertia number I; m is a parameter for regularization. Fourtakas and Rogers (2016) had examined the effect of m on the sediment stresses, and accordingly m is set to be 50 in the present study, a value at which the effect of regularization on sediment transport is negligible. Following Boyer et al. (2011) and Trulsson et al. (2012), the friction coefficient μ is estimated by

$$\mu = \mu_1 + \frac{\mu_2 - \mu_1}{1 + \sqrt{I_0 / I}} \tag{15}$$

and the inertia number I is determined by

$$I = \left(\frac{\alpha_{s0} - \alpha_s}{c_1 \alpha_s}\right)^2 \tag{16}$$

where, $\mu_1 = \tan\phi$ is the friction coefficient when $I = 0$ and the assembly is in static, with ϕ being the internal friction angle of the solid particles; μ_2 is the friction coefficient when I approaches infinite and the sediment moves extremely rapidly; I_0 is a model parameter; c_1 is the same parameter as in Eq. (12). In general, $\mu_2 = \tan\phi \sim 1.0$ and $\sqrt{I_0} = 0.1 \sim 0.3$ (Lee et al., 2016), and in this paper the values are determined according to a sensitivity analysis.

The present constitutive law can provide information on the pre-yield and post-yield regimes of the sediment phase, and thereby avoids the need of special technique for yield judgment (Pahar and Dhar, 2017; Zubeldia et al., 2018). When the assembly of solid particles is in quasi-static or static state, the stress related to the shear-rate-independent pressure p_s^e plays a similar role to the yield stress in Bingham and Herschel-Bulkley models (Fourtakas and Rogers, 2016). For unyielded sediment, the viscosity calculated by Eq. (14) is particularly large due to its zero shear rate, which then keeps the solid phase static.

2.3 Two-phase interactions

In the proposed model, the two-phase interactions are formulated in terms of the primary flow variables of the two phases. The pressure-gradient-related buoyancy on the solid particles is taken into account by the first term on the right side of Eq. (4), and other interphase forces are included in the term F_i in the momentum equations. Generally, F_i consists of drag force, virtual-mass force, lift force, etc (Drew, 1983). In a problem with high sediment concentration, the drag force is predominant (Hsu et al., 2004; Wang et al., 2016; Lee and Huang, 2018), and hence, for simplicity, here only drag force is considered. Assuming the drag force to be proportional to the relative velocity between the two phases, we have

$$F_i = \gamma \alpha_s \left(u_{f,i} - u_{s,i} \right) \tag{17}$$

in which, the coefficient γ can be estimated based on the formula proposed by Gidaspow (1994):

$$\gamma = \begin{cases} \dfrac{3}{4} C_D \dfrac{\rho_f \left| \mathbf{u}_f - \mathbf{u}_s \right|}{d_s} \alpha_f^{-1.65} & \alpha_s \leq 0.2 \\ 150 \dfrac{\alpha_s \rho_f \nu_f^0}{\alpha_f d_s^2} + 1.75 \dfrac{\rho_f \left| \mathbf{u}_f - \mathbf{u}_s \right|}{d_s} & \alpha_s > 0.2 \end{cases} \tag{18}$$

where, C_D is the drag coefficient for solid particles in an infinite fluid; $|\mathbf{u}|$ is the norm of the velocity vector; C_D is a function of the particle Reynolds number $\mathrm{Re}_s = \alpha_f \left| \mathbf{u}_f - \mathbf{u}_s \right| d_s / \nu_f^0$ and can be determined by the well-known Schiller and Naumann (1935) formula:

$$C_D = \begin{cases} \dfrac{24}{\mathrm{Re}_s} \left(1.0 + 0.15 \mathrm{Re}_s^{0.687} \right) & \mathrm{Re}_s < 1000 \\ 0.44 & \mathrm{Re}_s \geq 1000 \end{cases} \tag{19}$$

Note that Eq. (18) is considered to be more robust than the power law for γ used by Shi et al. (2017), which is based on the study of sediment settling in still water by Richardson and Zaki (1954) and is not valid for $\alpha_s \geq 0.4$ (Yin and Koch, 2007; Lee and Huang, 2018). The Gidaspow (1994) formula combines Wen and Yu (1966)'s power law for dilute suspensions and the Ergun equation, originally obtained by Ergun (1952) for pressure drop in the flow through packed columns and valid for dense solid-fluid mixtures. This formula has been well validated and widely applied to the study of intense sediment motion (Neri et al., 2003; Li et al., 2018; Si et al., 2018).

It is necessary to point out that, in the present model, the interphase momentum transfer term $-\left(\gamma \nu_f^t \, \partial \alpha_s / \partial x_i\right) / \left(\alpha_f \mathrm{Sc}\right)$ in the governing equations in Shi et al. (2017), which is due to the SPS turbulence and results from the Favre averaging in the spatial filtering, is neglected as it was found to play a negligible role in the simulations of both underwater granular column collapse and bed-erosion by dam-break flows.

2.4 Governing equations in Lagrangian form

The solid-liquid two-phase system is discretized into a single set of SPH particles, which move with the water velocity and carry properties of both phases. Hence, the substantial derivative of a physical quantity φ associated to a SPH particle is expressed as

$$\frac{d\varphi}{dt} \equiv \frac{\partial \varphi}{\partial t} + u_{f,j} \frac{\partial \varphi}{\partial x_j} \tag{20}$$

Note that the water is assumed to be weakly compressible, while the sediment is incompressible. Thus, the water density ρ_f is an unknown, while the sediment density ρ_s is a constant with $d\rho_s / dt = 0$. Rewriting the Eulerian form of the conservation equations (1) - (4) into Lagrangian form by virtue of Eq. (20), the governing equations for water density, sediment concentration, water velocity, and sediment velocity carried by a SPH particle are obtained as

$$\frac{d\left(\alpha_f \rho_f\right)}{dt} = -\left(\alpha_f \rho_f\right) \frac{\partial u_{f,j}}{\partial x_j} \tag{21}$$

$$\frac{d\alpha_s}{dt} = -\alpha_s \frac{\partial u_{f,j}}{\partial x_j} - \frac{\partial \left[\alpha_s \left(u_{s,j} - u_{f,j}\right)\right]}{\partial x_j} \tag{22}$$

$$\frac{du_{f,i}}{dt} = -\frac{1}{\rho_{f0}} \frac{\partial p_f}{\partial x_i} + \frac{1}{\alpha_f \rho_f} \frac{\partial \left(\alpha_f \rho_f T_{f,ij}\right)}{\partial x_j} + g_i - \frac{\gamma \alpha_s}{\alpha_f \rho_f} \left(u_{f,i} - u_{s,i}\right) \tag{23}$$

$$\frac{du_{s,i}}{dt} = -\frac{1}{\rho_s} \frac{\partial p_f}{\partial x_i} + \frac{1}{\alpha_s \rho_s} \frac{\partial \left(\alpha_s \rho_s T_{s,ij}\right)}{\partial x_j} + g_i + \frac{\gamma}{\rho_s} \left(u_{f,i} - u_{s,i}\right) - \left(u_{s,j} - u_{f,j}\right) \frac{\partial u_{s,i}}{\partial x_j} \tag{24}$$

where, $T_{k,ij}=\left(\tau^{0}_{k,ij}+\tau^{t}_{k,ij}\right)/\rho_k$ $(k=f,s)$.

The equation for the water density, i.e., Eq. (21), comes from the continuity equation for the water phase and describes the evolution of $\alpha_f\rho_f$ due to the volume change of the SPH particle. For the sediment concentration α_s, the continuity equation for the sediment phase is rewritten into Eq. (22), with the first term on the right side representing the contribution of the volume change of the SPH particle and the second term representing the effect of the inter-particle sediment mass flux. Note that as the velocities of the two phases are different, there may be mass and momentum fluxes of sediment among different SPH particles. Eqs. (23) and (24) are derived from the momentum conservation equations of the water and the sediment phases, respectively. The first four terms on the right side of the equations represent the effects of the fluid pressure, the viscous and turbulence stresses, the gravity, and the interphase drag force. The last term on the right side of Eq. (24) is a convection term for the inter-particle sediment momentum flux and is also a result of the relative velocity between the two phases.

2.5 SPH formulations

The detailed SPH formulations of the proposed two-phase model can be referred to Shi et al. (2017). Here, for completeness, a short description as well as some improvements in the discretizations of fluid stress term and inter-particle flux terms are presented. In a SPH model, the value of a physical quantity φ carried by SPH particle a, i.e., φ_a, is approximated by the summation over all neighboring particles in the supporting domain of the kernel function W:

$$\varphi_a=\sum_b \varphi_b W_{ab} V_b \tag{25}$$

in which, φ_b is the value of φ carried by the neighboring particle b; V_b is the volume of particle b defined by

$$V_b=\left(\frac{m_f}{\alpha_f\rho_f}\right)_b \tag{26}$$

with m_f being the water mass carried by the particle, which remains constant during the simulations; $W_{ab} = W\left(\left|\mathbf{x}_a - \mathbf{x}_b\right|, h\right)$, where $\mathbf{x}_a$ and $\mathbf{x}_b$ are the positions of particle a and b, respectively; h is the smoothing length of the kernel function W, and is set to be 1.3 times the initial particle spacing. In the present model, the quintic kernel function proposed by Wendland (1995) is utilized.

The volume of sediment phase carried by particle a, $\left(V_s\right)_a$, is given by

$$\left(V_s\right)_a = V_a\left(\alpha_s\right)_a = \left(\frac{m_f}{\alpha_f \rho_f}\right)_a \left(\alpha_s\right)_a \tag{27}$$

where, V_a is the volume of particle a. As time runs, the water mass m_f of particle a keeps constant, while the sediment mass $\left(m_s\right)_a = \rho_s\left(V_s\right)_a$ is variable. According to Eqs. (21) and (22), the volume of sediment carried by a SPH particle varies as a consequence of the inter-particle fluxes of sediment mass.

The divergence of the water velocity at particle a is discretized as

$$\left(\frac{\partial u_{f,j}}{\partial x_j}\right)_a = \sum_b \left[\left(u_{f,j}\right)_b - \left(u_{f,j}\right)_a\right]\left(\nabla_a W_{ab}\right)_j V_b \tag{28}$$

in which,

$$\nabla_a W_{ab} = \frac{\partial W}{\partial r}\frac{\mathbf{x}_a - \mathbf{x}_b}{\left|\mathbf{x}_a - \mathbf{x}_b\right|} \tag{29}$$

and $\left(\nabla_a W_{ab}\right)_j$ is its component in *j*-direction.

The symmetric scheme utilized in Violeau and Rogers (2016) which conserves momentum is adopted to formulate the fluid pressure terms, i.e., the first terms on the right side of Eqs. (23) and (24). Attention should be paid to the formulation of the shear stress terms, as α_s in the denominator may vanish when dealing with possible concentration discontinuity (Shi et al., 2017). In Eq. (30), the shear stress term is separated into a gradient term of stress and a gradient term of concentration. Replace $\left[\partial\left(\alpha_k \rho_k\right)/\partial x_j\right]/\left(\alpha_k \rho_k\right)$ by $\partial \ln\left(\alpha_k \rho_k\right)/\partial x_j$, which is a preferable form to increase the robustness of the model for problems with discontinuity of sediment concentration. Then, the symmetric scheme proposed by Ren et al. (2014) is applied. Hence,

$$\left[\frac{1}{\alpha_k\rho_k}\frac{\partial\left(\alpha_k\rho_k T_{k,ij}\right)}{\partial x_j}\right]_a=\left[\frac{\partial T_{k,ij}}{\partial x_j}+\frac{T_{k,ij}}{\alpha_k\rho_k}\frac{\partial\left(\alpha_k\rho_k\right)}{\partial x_j}\right]_a=\left[\frac{\partial T_{k,ij}}{\partial x_j}+T_{k,ij}\frac{\partial\ln\left(\alpha_k\rho_k\right)}{\partial x_j}\right]_a$$
$$=\sum_b\left[\left(T_{k,ij}\right)_a+\left(T_{k,ij}\right)_b\right]\left[1+\frac{1}{2}\ln\frac{\left(\alpha_k\rho_k\right)_b}{\left(\alpha_k\rho_k\right)_a}\right]\left(\nabla_a W_{ab}\right)_j V_b \tag{30}$$

An upwind scheme is proposed for the formulations of the inter-particle sediment mass flux term, i.e., the second term on the right side of Eq. (22), and sediment momentum flux term, i.e., the fifth term on the right side of Eq. (24):

$$\left\{-\frac{\partial\left[\alpha_s\left(u_{s,j}-u_{f,j}\right)\right]}{\partial x_j}\right\}_a$$
$$=-\sum_b\Big\{\left(\alpha_s\right)_a\max\left[\left(u_{s,j}-u_{f,j}\right)_a\left(\nabla_a W_{ab}\right)_j,0\right]+\left(\alpha_s\right)_a\max\left[\left(u_{s,j}-u_{f,j}\right)_b\left(\nabla_a W_{ab}\right)_j,0\right] \tag{31}$$
$$+\left(\alpha_s\right)_b\min\left[\left(u_{s,j}-u_{f,j}\right)_a\left(\nabla_a W_{ab}\right)_j,0\right]+\left(\alpha_s\right)_b\min\left[\left(u_{s,j}-u_{f,j}\right)_b\left(\nabla_a W_{ab}\right)_j,0\right]\Big\}V_b$$

$$\left[-\left(u_{s,j}-u_{f,j}\right)\frac{\partial u_{s,i}}{\partial x_j}\right]_a=\sum_b\left[\left(u_{s,i}\right)_a-\left(u_{s,i}\right)_b\right]\Big\{\min\left[\left(u_{s,j}-u_{f,j}\right)_a\left(\nabla_a W_{ab}\right)_j,0\right]$$
$$+\min\left[\left(u_{s,j}-u_{f,j}\right)_b\left(\nabla_a W_{ab}\right)_j,0\right]\Big\}V_b \tag{32}$$

Finally, the discretized SPH equations for sediment-water mixture flows become

$$\frac{d\left(x_i\right)_a}{dt}=\left(u_{f,i}\right)_a \tag{33}$$

$$\frac{d\left(\alpha_f\rho_f\right)_a}{dt}=-\left(\alpha_f\rho_f\right)_a\sum_b\left[\left(u_{f,j}\right)_b-\left(u_{f,j}\right)_a\right]\left(\nabla_a W_{ab}\right)_j V_b \tag{34}$$

$$\frac{d\left(\alpha_s\right)_a}{dt}=-\left(\alpha_s\right)_a\sum_b\left[\left(u_{f,j}\right)_b-\left(u_{f,j}\right)_a\right]\left(\nabla_a W_{ab}\right)_j V_b$$
$$-\sum_b\Big\{\left(\alpha_s\right)_a\max\left[\left(u_{s,j}-u_{f,j}\right)_a\left(\nabla_a W_{ab}\right)_j,0\right]+\left(\alpha_s\right)_a\max\left[\left(u_{s,j}-u_{f,j}\right)_b\left(\nabla_a W_{ab}\right)_j,0\right] \tag{35}$$
$$+\left(\alpha_s\right)_b\min\left[\left(u_{s,j}-u_{f,j}\right)_a\left(\nabla_a W_{ab}\right)_j,0\right]+\left(\alpha_s\right)_b\min\left[\left(u_{s,j}-u_{f,j}\right)_b\left(\nabla_a W_{ab}\right)_j,0\right]\Big\}V_b$$

$$\begin{aligned}\frac{d\left(u_{f,i}\right)_a}{dt} &= -\frac{1}{\rho_{f0}}\sum_b\left[\left(p_f\right)_a+\left(p_f\right)_b\right]\left(\nabla_a W_{ab}\right)_i V_b \\ &+\sum_b\left[\left(T_{f,ij}\right)_a+\left(T_{f,ij}\right)_b\right]\left[1+\frac{1}{2}\ln\frac{\left(\alpha_f\rho_f\right)_b}{\left(\alpha_f\rho_f\right)_a}\right]\left(\nabla_a W_{ab}\right)_j V_b \\ &+g_i-\frac{\gamma_a\left(\alpha_s\right)_a}{\left(\alpha_f\rho_f\right)_a}\left(u_{f,i}-u_{s,i}\right)_a\end{aligned}\tag{36}$$

$$\begin{aligned}\frac{d\left(u_{s,i}\right)_a}{dt} &= -\frac{1}{\rho_s}\sum_b\left[\left(p_f\right)_a+\left(p_f\right)_b\right]\left(\nabla_a W_{ab}\right)_i V_b \\ &+\sum_b\left[\left(T_{s,ij}\right)_a+\left(T_{s,ij}\right)_b\right]\left[1+\frac{1}{2}\ln\frac{\left(\alpha_s\right)_b}{\left(\alpha_s\right)_a}\right]\left(\nabla_a W_{ab}\right)_j V_b \\ &+g_i+\frac{\gamma_a}{\rho_s}\left(u_{f,i}-u_{s,i}\right)_a \\ &+\sum_b\left[\left(u_{s,i}\right)_a-\left(u_{s,i}\right)_b\right]\Big\{\min\left[\left(u_{s,j}-u_{f,j}\right)_a\left(\nabla_a W_{ab}\right)_j,0\right] \\ &+\min\left[\left(u_{s,j}-u_{f,j}\right)_b\left(\nabla_a W_{ab}\right)_j,0\right]\Big\}V_b\end{aligned}\tag{37}$$

with the following EOS for the water pressure

$$\left(p_f\right)_a=\frac{\rho_{f0}c_0^2}{\xi}\frac{\left(\alpha_f\rho_f\right)_a+\left(\alpha_s\right)_a\rho_{f0}}{\left(\alpha_f\rho_f\right)_a}\left\{\left[\frac{\left(\alpha_f\rho_f\right)_a+\left(\alpha_s\right)_a\rho_{f0}}{\rho_{f0}}\right]^{\xi}-1\right\}\tag{38}$$

Note that Eq. (33) determines the position of the SPH particle.

2.6 Time integration and Shepard filtering

The predictor-corrector scheme of Monaghan (1989) is adopted to integrate Eqs. (33) - (37) with respect to time. The time step is variable and restricted by the numerical sound speed, the maximum inertia forces, and the viscous forces of the two phases through the CFL conditions (Ulrich et al., 2013; Shi et al., 2017).

The strategy of Shepard filtering proposed by Shi et al. (2017) is utilized to damp the pressure oscillation in the sediment-water mixture. The filtering is performed every 20 time steps by reinitializing the water density of each particle according to

$$\left(\bar{\rho}_f\right)_a = \frac{\sum_b \left(\rho_f\right)_b W_{ab} V_b}{\sum_b W_{ab} V_b} = \frac{\sum_b \frac{\left(m_f\right)_b}{1-\left(\alpha_s\right)_b} W_{ab}}{\sum_b \frac{\left(m_f\right)_b}{\left(\alpha_f \rho_f\right)_b} W_{ab}} \tag{39}$$

Both the water mass and the sediment mass carried by a SPH particle are conserved in the Shepard filtering, resulting in

$$\left(\overline{\alpha_f \rho_f}\right)_a = \frac{\left(\alpha_f \rho_f\right)_a}{\left(\alpha_f \rho_f\right)_a + \left(\alpha_s\right)_a \left(\bar{\rho}_f\right)_a} \left(\bar{\rho}_f\right)_a \tag{40}$$

$$\left(\bar{\alpha}_s\right)_a = \frac{\left(\alpha_s\right)_a}{\left(\alpha_f \rho_f\right)_a + \left(\alpha_s\right)_a \left(\bar{\rho}_f\right)_a} \left(\bar{\rho}_f\right)_a \tag{41}$$

2.7 Boundary conditions

In SPH models, free water surface can be naturally tracked by particles but special attention should be paid to the solid wall boundaries. In the present model, the dynamic boundary condition proposed by Crespo et al. (2007) is employed to avoid the kernel truncation near the solid boundaries. The solid boundary is represented by allocating three layers of SPH particles along it, which satisfy the same equations as those for the fluid particles but do not move in response to the computed forces exerted on them. They keep fixed in position for immobile boundaries or move according to externally imposed trajectory for prescribed moving boundaries.

2.8 Numerical implementations

The proposed model is implemented on the basis of the open-source SPH package GPUSPH, which was originally developed by Hérault et al. (2010). GPUSPH is programmed with CUDA and C++, and conducts parallel computations on Nvidia CUDA-enabled Graphics Processing Units (GPUs). The numerical computations in the present study are carried out on an Nvidia Tesla K40c GPU with 2880 processor cores.

3 Collapse of underwater granular columns

Collapse of a submerged granular column under gravity is a classical problem of massive sediment motion in free surface flows, which occurs in a variety of natural and hazardous processes such as underwater landslide and submarine avalanches (Rondon et al., 2011). It has also been widely used as a benchmark problem for validation of numerical models for dense granular motion in fluid (Meruane et al., 2010; Savage et al., 2014; Wang et al., 2017a; Si et al., 2018). However, the relevant collapsing process is still not well understood. During collapse, the sediment phase may be fluid-like, solid-like or in a transition state according to its shear rate, which makes modelling the behavior of the granular column very difficult. The solid-fluid interactions make the situation even more complicated. The variation of the fluid pressure in the porous material can either stabilize or destabilize the assembly of particles (Iverson et al., 2000), and the drag force between the solid particle and the fluid may resist or accelerate the collapsing process of the granular column depending on the relative velocity between the two phases (Si et al., 2018). The initial volume fraction of the solid phase plays a very important role in the phenomenon (Rondon et al., 2011; Wang et al., 2017b). In this section, the proposed two-phase SPH model is carefully validated and employed to investigate the effects of water-sediment interactions on the collapse of loosely/densely packed granular columns submerged in still water. Effects of the free surface motion are discussed as well.

Rondon et al. (2011) had conducted a well-known experimental study on the role of initial porosity in the case of a granular column collapse in a viscous fluid. Due to the large fluid viscosity and the low ratio of the column height to the fluid depth in Rondon et al. (2011), the motion of the free surface resulting from the granular column collapse was negligible. Following Rondon et al. (2011), Wang et al. (2017b) performed a similar experiment with a larger granular column size and using water as the ambient fluid. In this experiment, the fluctuation of free water surface was visible, though not significant. In the present study, the proposed two-phase SPH model is applied to the experiment of Wang et al. (2017b).

The experiment of Wang et al. (2017b) was conducted in a rectangular tank of

50cm-long, 10cm-wide, 15cm-high as shown in Figure 1. A granular column was initially confined at the left end of the tank by a removable gate. The horizontal and the vertical directions are defined as x (i.e., x_1 in the governing equations) and z (i.e., x_3 in the equations) directions, respectively. L is the distance from the left end of the tank to the front of the granular avalanche, and H is the height of the column at $x = 0$. The particles used were glass beads of density $\rho_s = 2500\,\mathrm{kg/m^3}$ and mean diameter $d_s = 300\,\mu\mathrm{m}$, with an internal friction angle of $\phi = 25^\circ \pm 0.4^\circ$. The granular column was prepared in both loose-packing and dense-packing state. In the loose-packing case, the glass beads were gently poured into the space delimited by the wall and the gate, resulting in an initial shape of $L \times H = 6\,\mathrm{cm} \times 8\,\mathrm{cm}$ granular column. The initial sediment volume fraction of the loosely-packed column was $\alpha_s = 0.53 \pm 0.005$. In the dense-packing case, the tank was gently tapped and an initial solid volume fraction of $\alpha_s = 0.57 \pm 0.003$ was obtained. The initial length of the column L was $6\,\mathrm{cm}$, and the initial height of the column H was reduced to $7.8\,\mathrm{cm}$. The granular column was submerged in 10-cm-deep water (with fluid density $\rho_f = 1000\,\mathrm{kg/m^3}$ and viscosity $\nu_f^0 = 10^{-6}\,\mathrm{m^2/s}$). The time period taken to remove the gate was shorter than 0.1 s and its influence on the column collapse could be ignored (Wang et al., 2017b). Once the gate was removed, the column collapsed and the final deposition of the granular mass was reached in just a few seconds.

The physical problem as described above can be treated as a two-dimensional problem. To simulate such a problem with a three-dimensional numerical model, the computational conditions are kept the same as those in the experiments, except in the width direction of the tank (y direction), for which a periodic condition is imposed and a minimum 4 layers of SPH interpolating particles are arranged. The initial size of SPH interpolating particles is set to be 0.002 m according to a convergence study, and in the present simulations, the solid-fluid mixture is discretized into a set of $250 \times 50 \times 4 = 50000$ SPH particles. Besides, the dynamic boundary condition is applied to the bottom and the sidewalls in x direction, with three layers of fixed SPH particles representing the solid boundaries. Hence, in each computation, a total of 50000 interpolating particles for the two-phase mixture and 4464 particles for the solid boundaries are used. Figure 2 shows the particle configuration at $t = 0\,\mathrm{s}$ after removal of the gate in the loose-packing case, in which the red particles are those carrying the initial sediment volume fraction 0.53 and represent the saturated granular column. Values of the model parameters and some physical quantities of the solid material used in the present simulations are summarized in Table 1. The sensitivities of the granular avalanche front position L at t = 0.5 s in the loose-packing case and the column height H at t = 4.0 s in the dense-packing case to model parameters are shown in Table 2. It is seen that the numerical results are not significantly affected by a variation of the parameters as long as the variation is limited in the specified range. The parallel computations are carried out on an CUDA-enabled Nvidia Tesla K40c GPU, and it requires about 25 minutes of computational time to simulate 1 second of the physical experiment.

3.1 Model validations

Figures 3 and 4 show the comparisons of the computed profiles of the granular column by the present model with the experimental data for the loose-packing and dense-packing cases, respectively. Results of the earlier two-phase SPH model developed by Shi et al. (2017) are also presented. The predictions by the present proposed model are generally in good agreement with the experimental data in both cases and are much more accurate than those by the model of Shi et al. (2017). Small discrepancies are observed at $t = 0.5\,\mathrm{s}$ in the loose-packing case and at $t = 1.0\,\mathrm{s}$ in the dense-packing case, but they are still acceptable. For the loosely-packed column, upon the removal of the gate, the whole upper part falls immediately, leading to a thin surge of solid materials at the front of the granular mass. The flow front moves quickly and stops at $x = 22.0\,\mathrm{cm}$ with a long runout distance L. Simultaneously, the grains in the main body of the column flow down the surface, and a triangular final deposition profile is reached in 2.5 seconds. For the dense-packing case, a very different collapsing process is observed. Once the gate is removed, particles at the upper right corner and on the lateral surface fall freely, resulting in a steep profile with a round corner before $t = 1.0\,\mathrm{s}$. The left upper part of the column keeps unmoved at the initial stage and assumes a plateau-like shape. As time goes on, the erosion propagates inward, and the plateau is eroded gradually. The flow front stops at $x = 18.0\,\text{cm}$ in 1.5 seconds, with a shorter runout distance than that in the loose-packing case. A bump is formed behind the flow front, and the concave region between the column body and the bump is filled gradually by the particles falling down from the top of the column. This so-called "hydraulic-like granular jump" behavior shown in the experiment (Wang et al., 2017b) is captured by the proposed model. The final deposition profile of the initially densely packed column is obtained after 4.0 seconds, implying a longer collapse duration than that in the loose-packing case.

Figures 5 and 6 show the sequential configurations of the free water surface for the loose-packing and the dense-packing cases, respectively. Compared with the observed surface motion in the original video records (available from the web version of Wang et al. (2017b)), the simulated fluctuations of the free water surface are consistent with the experimental results. Also as expected, the water surface fluctuation in the dense-packing case is smaller than that in the loose-packing case due to a slower collapsing process. Specifically, at the initial stage, the collapsing column pulls down the water surface. The free surface is thus disturbed and the wave propagates back and forth in the tank until it dissipates due to the fluid viscosity.

The evolutions of the solid volume fraction carried by the SPH particles in the two cases are shown in Figures 5 and 6. For the loose-packing case, as shown in the dark-colored zone at the lower left corner of the granular pile, the maximum solid volume fraction of the column increases from the initial value of 0.53 to about 0.55 in the early collapse stage and keeps increasing gradually as time goes on, indicating a contraction behavior of the loosely-packed column. On the contrary, for the dense-packing case, the value decreases from 0.57 to 0.56 in the initial stage, presenting a dilation behavior of densely packed materials. The result of the contraction/dilation of the granular column is consistent with that found in Rondon et al. (2011), Wang et al. (2017b), and Lee and Huang (2018), further validating the present two-phase SPH model. In addition, the suspension of solid particles around the flow front is well captured by the present model, as shown in Figures 5(b) and 6(b). The particles are suspended by the water vortices when rapid collapse occurs in the early stage of the process, and soon settle down as the granular flow propagates. This phenomenon is clearly shown in the original video records as shown in Figure 7.

3.2 Water-sediment interactions

~~As shown in the previous section, the behaviors of the initially loosely packed and the densely packed columns are significantly different. In this section, the calculated fluid pressure and the interphase drag force are presented, and the effects of the water-sediment interactions on the collapse of loosely/densely packed underwater granular columns are investigated.~~

Figure 8 shows the distributions of the fluid pressure of the SPH particles in both the early and the final collapse stages for the loose-packing case, and Figure 9 for the dense-packing case. Note that the initial hydrostatic water pressure at the bottom of the tank is $\rho_f gh = 981\,\mathrm{Pa}$ ~~above the legend is added to indicate the initial hydrostatic water pressure at the bottom of the bank~~. For the loose-packing case, the fluid pressure in the lower part of the column increases due to the contraction of the granular material in the early stage of the collapse, with a maximum value of 1200 Pa reached. The high pressure disperses with the spreading of the granular mass. However, for the dense-packing case in Figure 9, a large low-pressure zone is observed in the column at the initial collapse stage, and it lasts for quite some time. It should be pointed out that fully restoration of the water pressure to the hydrostatic condition is not pursued in the present simulations due to a considerable increase of the computational efforts. It is shown that the numerical results of the fluid pressure are consistent with those of Wang et al. (2017b) and Si et al. (2018). The gradient of the fluid pressure field produces a force on the solid phase. High pressure within the column in the loose-packing case then leads to an outward force on the solid phase that accelerates the collapse, while low pressure in the densely packed column leads to an inward force that helps to stabilize the granular column. Note that in Figure 8(a), due to lowering of the free water surface, the fluid pressure within the upper column becomes smaller ~~is lower~~ than the hydrostatic value at the same height. This result is physically more realistic than that of Si et al. (2018) and Lee and Huang (2018), in which the rigid-lid hypothesis is imposed on the water surface and thus the motion of the free surface is neglected.

Effects of the interphase drag force on the granular column collapse are presented in Figures 10 and 11. The distributions of the computed drag force at representative times in the two cases are shown in Figure 10. $\mathbf{F}_{\mathrm{d}} = \gamma\alpha_s\left(\mathbf{u}_f - \mathbf{u}_s\right)$, and its norm $\left|\mathbf{F}_{\mathrm{d}}\right|$ is normalized by $\rho_s g$. In both cases, at the initial collapse stage, the water is pulled down from a static state by the grains that are about to crush. This in turn exerts a strong drag force on the solid particles, which points inward to the core of the column and hinders the collapse. The magnitude of the drag force near the column surface where the particles move rapidly is generally larger than that in the inner zone. At the initial stage of collapse, the magnitude of the drag force in the densely packed column (with a maximum value of about $0.30\rho_s g$) is much larger than that in the loosely packed one (with a maximum value of $0.14\rho_s g$), resulting in a more stable state of the granular mass in the dense-packing case. Besides, in the later stage when the magnitude of the drag force decreases with the deceleration of the collapse, the drag force in the main part of the densely packed column at $t = 2.4\,\mathrm{s}$ is still stronger than that in the loosely packed material at $t = 1.0\,\mathrm{s}$. Notably, different from the situation in the main body of the column where the interphase drag helps to stabilize the granular column, in the flow front the drag force on the solid particles may show a positive effect and drive the granular flow, as shown in the zoomed-in view in Figure 10(b). Due to the stronger effect of the drag force in the flow front, the granular flow in the loose-packing case has a longer runout distance than that in the dense-packing case.

To further identify the effects of the interphase drag force, more simulations of the collapse are carried out using the present model but excluding the drag force. $\gamma = 0$ is set, while the values of all the other parameters and coefficients are kept the same as in the above computations. Figure 11 shows comparisons of the computed sequential profiles of the granular column with and without the formulation of the drag force. In both the loose-packing and the dense-packing cases, when ignoring the drag force, the columns move faster at the initial collapse stage, with a wider spread of the particles and a smaller column height H at the left end of the tank. However, in the later stage, for the loosely packed column the drag force on the solid particles drives the front part of the granular flow, as shown in the comparisons at $t = 1.0$ s and $t = 2.5$ s in Figure 11(a). The situation is different for the dense-packing case where the positive effect of the drag force is insignificant. In almost the entire period of the collapse, the column simulated without the drag effects has a larger runout distance than that including the interphase drag. Neglect of the drag force results in a longer duration of collapse in both cases. The computed profiles of the deposit without the drag force for both loose and dense packing cases are quite similar as shown in Figures 11(a) and 11(b), which demonstrates that the importance of the initial solid volume fraction on column collapsing process can be revealed only when the water-sediment drag is properly taken into account.

3.3 Evolution of ~~water~~ vortices generated by granular column collapse

~~The simulated evolutions of the water vortices are shown in Figures 12 and 13 to help understand the two-phase problem better as very few similar studies contain the results of the vortex evolution and the fluid flow within the porous materials.~~

The simulated evolutions of vortices generated by the granular column collapse are shown in Figures 12 and 13. Well representation of the dynamic process of these vortices is an advantage of the present numerical model. It is shown that at the initial stage of the collapse, a large vortex is induced by the movement of the solid grains. For the loose-packing case, the vortex core is around the upper right corner of the column, and the water velocity in the whole upper column is notable, as shown in Figure 12(a). On the other hand, for the dense-packing case in Figure 13(a), the vortex core is around the right-side surface of the column, implying that the column collapse starts from the right side of the surface and propagates inward. The moving layer of the water flow within the granular mass in the loose-packing case is much thicker than that in the dense-packing case. During the later stage of the collapse process in both cases, the vortex propagates and grows with the acceleration of the collapse as shown in Figures 12(b) and 13(b). Once the front of the granular flow stops, the vortex moves upward and finally disappears due to the fluid viscosity.

The vortex can induce suspension of solid particles. The areas encircled in Figures 5(b) and 6(b) for the particle suspension are in the core of the vortices, as shown in Figures 12(b) and 13(b). The vortex may also be affected by the fluctuation of free water surface. In Figure 12(a), the vortex is restricted by the free surface, and the sinking of the surface increases the velocity of the water flowing into the upper part of the porous material, resulting in a downward drag force on the solid particles in the upper column as shown in Figure 10(a).

4 Sediment transport by dam-break flows

Dam break over a movable bed may cause a significant amount of sediment to be eroded and transported, leading to substantial changes of the downstream river morphology and possible damages to infrastructures. It has long been the subject of many experimental and numerical studies in hydraulic and river engineering (Capart and Young, 1998; Ran et al., 2015). It is also a test case for meshless numerical models of sediment transport (Shakibaeinia and Jin, 2011; Ulrich et al., 2013; Pahar and Dhar, 2017; Zubeldia et al., 2018). However, due to the violent free-surface motion and the complex bed-erosion process, development of a comprehensive numerical model for detailed description of the dam-break erosion is still very challenging (Shakibaeinia and Jin, 2011). In this section, the proposed two-phase SPH model is applied to the massive sediment transport caused by dam-break flows to assess its predicative capability.

The case considered is the two-dimensional experiment of dam break over a mobile-bed carried out by Spinewine (2005), which has been widely used to validate numerical models for bed erosion caused by dam-break flows (Ran et al., 2015; Pahar and Dhar, 2017). The experiment was conducted in a 6-m-long flume, where the bottom was covered by a layer of saturated movable sediment material. As shown in Figure 14, a clear water column with a height h_f of 0.40 m was initially blocked by a gate located at the middle of the flume. The initial thickness of the saturated sediment directly below the clear water was h_{s1} = 0.07 m, while that of the saturated bed on the downstream side of the gate was h_{s2} = 0.12 m. Thus, an upward step made up of movable sediment particles was assumed. The bed material was cylindrical PVC pellets, which had a median equivalent spherical diameter of 3.9 mm, a specific density of 1580 kg/m^3, a friction angle ϕ of 38°, and no cohesion. Before lifting the gate, the PVC pellets were initially compacted to the random close-packing concentration α^* equal to 0.58.

The computational conditions except those in the width direction of the flume are the same as those in the experiment. Similar to the simulations of the two-dimensional underwater granular column collapse, the periodic boundary condition is imposed in the width direction, and 4 layers of SPH interpolating particles are initially placed along the flume width for the three-dimensional computations. The dynamic boundary condition is applied to the bottom and the sidewalls in x direction, and three layers of SPH particles are fixed to represent the solid boundaries. The initial size of the SPH interpolating particles is 0.01 m, and a total of 79272 particles are utilized in the whole computational domain. The initial sediment volume fraction carried by the SPH particles in the movable bed is set to be the experimental value. The gate is instantaneously removed, and the effect of the time to remove the gate is neglected. A sensitivity study on the dam-break flow leading position at t = 0.50 s is conducted as shown in Table 2. Values of the model parameters used in the present simulation are summarized in Table 1. The GPU-based parallel computation takes about 90 minutes to simulate 1 second of the physical experiment, with a variable time step of about 4×10^{-6} s.

4.1 Model validations

Figure 15 shows the comparisons between the computed and the observed interfaces separating the three characteristic flow regions: a clear water layer, a moving bed layer with intense sediment transport and the static sediment bed. ~~profiles of the free water surface and the eroded bed at representative times.~~ General agreement between the numerical and the experimental results of all the interfaces ~~both the water surface and the sediment bed~~ is reasonable, especially for the water surface and the surface of the moving bed in the regions near the gate, such as at $x = 0 - 0.6$ m in Figure 15(b) and at $x = 0 - 1.0$ m in Figure 15(d). At the front of the dam-break wave, the simulated interfaces ~~computed profiles of the water~~

~~surface and the sand bed~~ are also broadly comparable to the experimental results. However, at $t = 0.25$ s, a comparatively large error appears in the profiles of both the water surface and the moving bed layer ~~granular bed~~, which is believed to be caused by the neglect of the effect of gate removal. Fortunately, the gate removal effect diminishes rapidly with the propagation of the dam-break wave, as shown in Figures 15(b)-15(f) (Fu and Jin, 2016). On the movable bed, both humps and troughs are well captured, which supports the rheology-based constitutive law used in the model.

~~The proposed model is shown to be capable of predicting the characteristic flow and sediment parameters relevant to engineering practice. The computed values of the flow~~ Numerical results for the leading position of the flow and the maximum bed height at typical instants of time are compared with the experimental data in Table 3 ~~Table 2~~. It is shown that the model accurately predicts the leading position of the dam-break flow at all the typical instants except at $t = 0.25$ s, with a mean error of 0.8%. Prediction of the maximum bed height is also reliable with a mean error of 12.9%~~, even though the accuracy is lower than that of the predicted flow leading edge position~~.

For a further verification of the present model, a flat bed case, i.e., a case in which the thickness of the saturated bed is the same on both upstream and downstream side of the gate, or, $h_{s1} = h_{s2} = 0.12$ m, is simulated. In the experiment, the initial height of the clear water column is $h_f = 0.35$ m. The vertical profiles of the longitudinal velocity are measured in the range from $x = -0.95$ m to the wave front with a spacing of 0.1 m. Similar to the results shown in Figure 15, the computed interfaces at all the typical instants are in good agreement with the experimental data, except at $t = 0.25$ s. A similar presentation of figures is thus omitted for concision. In Figure 16, comparisons of the horizontal velocity are made while the computed interfaces are also plotted. Generally, the computed velocity profiles agree very well with the measured data except at certain positions close to the wave front. In the clear water layer, the horizontal velocity is shown to be rather uniform, and in the moving bed layer, it decreases nearly linearly with depth and becomes zero at the top of the static bed. Evolution of the movable bed is also well represented by the proposed numerical model.

4.2 Two-phase interactions during bed erosion

In this subsection, ~~to study the water-sediment interactions and further reveal the underlying mechanisms in the bed erosion,~~ numerical results on fluid pressure, sediment concentration, velocities of the two phases and interphase drag force at three different stages of dam-break erosion, namely, the initial stage, the intermediate stage and the final stage, are discussed for a better understanding of the water-sediment interactions and the underlying mechanisms in the bed erosion.

4.2.1 Initial stage

Figure 17 ~~16~~ is the snapshot of particle configuration, along with the distribution of sediment concentration carried by the SPH particles, and the pressure at $t = 0.15\,\text{s}$. Even though the computed bed profiles before $t = 0.25\,\text{s}$ are not accurate enough due to the effect of the gate removal, which is neglected in the numerical model, the numerical results are still indicative of the dynamics of bed erosion at the initial stage. Figure 18 ~~17~~ shows the distributions of the water velocity in the fluid column and in the granular material, the sediment velocity over the granular bed, and the drag force on the solid phase. The dotted line in Figure 17(b) ~~16(b)~~ and the dashed lines in Figure 18 ~~17~~ represent the top of the moving bed layer ~~the bed surface~~, obtained according to the particle configuration in Figure 17(a) ~~16(a)~~.

Immediately after the gate is removed, the water in the upper part of the column falls down and the toe of the water column moves with a maximum velocity of 2.5 m/s. The water pushes the solid particles on the bed surface to move forward, and pulls the particles and the fluid in the granular material upward. The bed particles are washed out with a maximum particle velocity of 2.1 m/s, and the velocity of the fluid flow in the granular material is notable as well. Note that before removing the gate, the hydrostatic fluid pressure in the bed on the upstream side of the gate is much larger than that in the bed downstream. This discontinuity of pressure at the gate position disappears rapidly once the gate is removed. This process is well simulated by the present model as shown in Figure 17(b) ~~16(b)~~, where the computed fluid pressure across the dotted interface is continuous with no apparent fluctuation, which demonstrates the capability of the present SPH model in predicting fluid pressure accurately.

The interphase drag and the fluid pressure play an important role in the bed erosion. Figure 18(b) ~~17(b)~~ marks the region in which the magnitude of the dynamic pressure force $\left|-\alpha_s \nabla p_f^{\mathrm{d}}\right| = \left|-\alpha_s \nabla p_f + \alpha_s \rho_s \mathbf{g}\right|$ is larger than $0.6\rho_s g$ ($\mathbf{g}$ is the gravitational acceleration). The vector in Figure 18(c) ~~17(c)~~ represents the drag force, while the contour stands for the ratio of the magnitude of the drag force to that of the dynamic pressure force. The contour line of $\left|\mathbf{F}_{\mathrm{d}}\right| / \left|-\alpha_s \nabla p_f^{\mathrm{d}}\right| = 1$ is drawn to show the area where the interphase drag is stronger than the dynamic pressure force. It shows that at the initial stage of the dam-break erosion, the magnitudes of the drag force and the dynamic pressure force are quite large, with a value more than $0.5\rho_s g$ near the gate position. The drag force plays a greater role near the bed surface at the toe of the water column, while the dynamic pressure force is more important at the leading edge of the dam-break wave.

4.2.2 Intermediate stage

Figure 19 ~~18~~ shows the particle configuration and the computed pressure at $t = 0.70\ \mathrm{s}$, and Figure 20 ~~19~~ presents the distributions of water velocity, sediment velocity, and interphase drag force. The lines, marks, and contours are included with the same meanings as in Figures 17 ~~16~~ and 18 ~~17~~. ~~More information can be found in the above subsection.~~

In Figure 19(a) ~~18(a)~~, humps and troughs on the granular bed are formed. Sediment suspension is observed mainly on the lee side of the humps. In Figure 19(b), ~~18(b)~~ a high pressure zone is observed at the leading edge of the flow, which is a result of the dam-break wave impacting on the granular bed. It is noticed that the bumps in the pressure distribution fall behind the humps on the bed, implying the push of water on the humps. The dam-break flow propagates with more water involved. At $t = 0.70\ \mathrm{s}$, a massive amount of water pours downstream with a maximum velocity larger than 2.5 m/s. It is shown in Figure 20(a) ~~19(a)~~ that the velocity in the free-water layer above the bed in the downstream region ($x > 0\ \mathrm{m}$) is almost invariant in the vertical direction ~~vertically constant~~, consistent with the results of Ran et al. (2015) and Spinewine and Capart (2013). Inside the granular bed, the water velocity decreases rapidly towards the bottom. In addition, the streamlines have a similar shape of the interface between the water and the moving bed layer ~~bed surface~~. Bed materials flow with the water, and the magnitude of the sediment velocity on the lee side of the hump seems to be larger than that on the front side.

It is shown in Figures 19(b) ~~18(b)~~ and 20(b) ~~19(b)~~ that the impact on the bed by the dam-break wave results in a notable region where the dynamic pressure force plays a significant role. In Figure 20(c) ~~19(c)~~, the magnitude of the drag force is not as large as that in Figure 18(c) ~~17(c)~~. The regions encircled by the contour line where the drag force is greater than the dynamic pressure force are located mainly in the troughs, where an active sediment suspension exists. Inside the granular bed, it seems that the dynamic pressure force plays a more important role than the interphase drag force.

4.2.3 Final stage

Figures 21 ~~20~~ and 22 ~~21~~ show the results of dam-break erosion at $t = 1.50\,\mathrm{s}$, i.e., in the final stage. In Figure 21(a) ~~20(a)~~, more sediment is suspended especially in the front part of the flow, consistent with the observed turbidity above the bed in the experimental flow. The bed particles are washed away, and the humps are eroded. The computed pressure is continuous and reasonable. Some high-pressure zones occur at the leading edge of the dam-break flow as it can be seen in Figure 21(b) ~~20(b)~~ and similarly large-dynamic pressure force zone is marked in Figure 22(b) ~~21(b)~~.

The water velocity in the front part of the dam-break flow is still quite large, and it is the same for the sediment velocity near the leading edge of the flow. Similar to the situation in the intermediate stage, the interphase drag force is weak inside the granular material but quite strong near the moving bed surface. The regions where the magnitude of the drag force is larger than that of the dynamic pressure force are corresponding to the regions where active sediment suspension exists.

5 Conclusions

An improved two-phase SPH model based on the continuum formulation ~~description~~ of solid-liquid mixtures is proposed for massive sediment motion in free surface flows, providing a unified description of gravity-induced subaqueous granular flows and shear flow driven intense sediment transport. A constitutive law based on the rheology of dense granular flows for the intergranular stresses of the solid phase and a drag force formula that combines the power law for dilute suspensions and the Ergun equation for dense solid-liquid mixtures are adopted. For numerical solutions, the governing equations are solved in a distinctive two-phase SPH framework ~~discretized with the weakly compressible SPH formulation schemes~~, and the numerical model is implemented in CUDA and C++. The parallel computations are conducted on CUDA-enabled GPUs.

The model is employed to investigate the collapses of both loosely and densely packed columns in water. The computed profiles of the granular columns during the entire collapsing process are in very good agreement with the experimental data, and the computed distributions of sediment concentration are also consistent with the experimental observations. The behaviours of the loosely packed and the densely packed columns are found to be significantly different and, based on the computed results of fluid pressure and interphase drag force along with the evolution of water vortices, it is shown that a much lower pressure and a stronger interphase drag force in the densely packed column lead to a more stable state of the granular mass in the dense-packing case.

In the case of dam-break flows, the computed profiles of the free water surface and the movable bed as well as the numerical results for the leading position of the flow and the maximum bed height are compared with the measured results. It is shown that the numerical results are in good agreement with the experimental data. Furthermore, to study the water-sediment interactions during the bed erosion process, the water pressure, sediment concentration, velocities of the two phases, and interphase drag force in the early, intermediate, and final stages of the dam-break erosion are computed. The numerical results indicate that at the initial stage of erosion, the interphase drag plays a greater role near the bed surface at the toe of the water column, while the dynamic pressure force is more important at the leading edge of the dam-break flow. In the intermediate and the final stages, the drag force is greater than the dynamic pressure force in the regions where active sediment suspension exists, while inside the granular bed, the dynamic pressure force seems to play a more important role.

In summary, it is shown that the proposed two-phase SPH model successfully describes both the gravity-induced underwater granular flows and the intense sediment transport by flowing water and reasonably represents the physics of massive sediment motion in water. Further applications of the model to certain practical scenarios in which the two kinds of flows exist simultaneously such as landslides triggered by storm in shallow sea and flows resulted in barrier or dam breaks are thus highly possible.

Acknowledgments

This work is jointly supported by National Key Research and Development Program, MOST, China under grant No. 2018YFC0407506, projects from EPSRC (EP/R02491X/1), and Open Research Fund Program of State Key Laboratory of Hydroscience and Engineering (sklhse-2019-B-01). The proposed two-phase SPH model is implemented on the basis of the open source GPUSPH code developed by Alexis Hérault, Giuseppe Bilotta, and Robert A. Dalrymple, and the authors thank all the contributors.

References

Bakhtyar R., Barry D.A., Yeganeh-Bakhtiary A., Li L., Parlange J.-Y., Sander G.C., 2010. Numerical simulation of two-phase flow for sediment transport in the inner-surf and swash zones. Advances in Water Resources, 33, 277-290.

Boyer F., Guazzelli É, Pouliquen O., 2011. Unifying suspension and granular rheology. Physical Review Letters, 107, 188301.

Bui H.H., Sako K., Fukagawa R., 2007. Numerical simulation of soil-water interaction using smoothed particle hydrodynamics (SPH) method. Journal of Terramechanics, 44(5), 339-346.

Capart H., Young D.L., 1998. Formation of a jump by the dam-break wave over a granular bed. Journal of Fluid Mechanics, 372, 165-187.

Chauchat J., 2018. A comprehensive two-phase flow model for unidirectional sheet-flows. Journal of Hydraulic Research, 56(1), 15-28.

Chen X., Li Y., Niu X., Chen D., Yu X., 2011. A two-phase approach to wave-induced sediment transport under sheet flow conditions. Coastal Engineering, 58(11), 1072-1088.
Chiodi F., Claudin P., Andreotti B., 2014. A two-phase flow model of sediment transport: transition from bedload to suspended load. Journal of Fluid Mechanics, 755, 561-581.
Crespo A.J.C., Gómez-Gesteira M., Dalrymple R.A., 2007. Boundary conditions generated by dynamic particles in SPH methods. Computers Materials & Continua, 5(3), 173-184.
Dalrymple R.A., Rogers B.D., 2006. Numerical modeling of water waves with the SPH method. Coastal Engineering, 53(2-3), 141-147.
Dong P., Zhang K., 1999. Two-phase flow modeling of sediment motions in oscillatory sheet flow. Coastal Engineering, 36, 87-109.
Dong P., Zhang K., 2002. Intense near-bed sediment motions in waves and currents. Coastal Engineering, 45, 75-87.
Drew D.A., 1983. Mathematical modeling of two-phase flow. Annual Review of Fluid Mechanics, 15(1), 261-291.
Ergun S., 1952. Fluid flow through packed columns. Chemical Engineering Progress, 48, 89-94.
Fourtakas G., Rogers B.D., 2016. Modeling multi-phase liquid-sediment scour and resuspension induced by rapid flows using Smoothed Particle Hydrodynamics (SPH) accelerated with a Graphics Processing Unit (GPU). Advances in Water Resources, 92, 186-199.
Fu L., Jin Y.C., 2016. Improved multiphase Lagrangian method for simulating sediment transport in dam-break flows. Journal of Hydraulic Engineering, ASCE, 142(6), 04016005.
Gidaspow D., 1994. Multiphase flow and fluidization: Continuum and kinetic theory descriptions. Academic Press, San Diego.
Gotoh H., Khayyer A., 2018. On the state-of-the-art of particle methods for coastal and ocean engineering. Coastal Engineering Journal, 60(1), 79-103.
Hérault A., Bilotta G., Dalrymple R.A., 2010. SPH on GPU with CUDA. Journal of Hydraulic Research, 48(S1), 74-79.
Hsu T.J., Jenkins J.T., Liu P.L.F., 2004. On two-phase sediment transport: sheet flow of massive particles. Proceedings of the Royal Society A – Mathematical Physical and Engineering Sciences, 460(2048), 2223-2250.
Iverson R.M., Reid M.E., Iverson N.R., LaHusen R.G., Logan M., Mann J.E., Brien D.L., 2000. Acute sensitivity of landslide rates to initial soil porosity. Science, 290(5491), 513-516.

Johnson P.C., Jackson R., 1987. Frictional-collisional constitutive relations for granular materials, with application to plane shearing. Journal of Fluid Mechanics, 176, 67-93.

Keating B.H., McGuire W.J., 2000. Island edifice failures and associated tsunami hazards. Pure and Applied Geophysics, 157(6-8), 899-955.

Lee C.H., Huang Z., 2018. A two-phase flow model for submarine granular flows: With an application to collapse of deeply-submerged granular columns. Advances in Water Resources, 115, 286-300.

Lee C.H., Low Y.M., Chiew Y.M., 2016. Multi-dimensional rheology-based two-phase model for sediment transport and applications to sheet flow and pipeline scour. Physics of Fluids, 28(5), 053305.

Li J., Cao Z., Hu K., Pender G., Liu Q., 2018. A depth-averaged two-phase model for debris flows over erodible beds. Earth Surface Processes and Landforms, 43, 817-839.

Lynett P., Liu P.L.F., 2002. A numerical study of submarine-landslide-generated waves and run-up. Proceedings of the Royal Society of London A, 458, 2885-2910.

Mayrhofer A., Laurence D., Rogers B.D., Violeau D., 2015. DNS and LES of 3-D wall-bounded turbulence using Smoothed Particle Hydrodynamics. Computers and Fluids, 115, 86-97.

Meruane C., Tamburrino A., Roche O., 2010. On the role of the ambient fluid on gravitational granular flow dynamics. Journal of Fluid Mechanics, 648, 381-404.

Monaghan J.J., 1989. On the problem of penetration in particle methods. Journal of Computational Physics, 82(1), 1-15.

Neri A, Ongaro T.E., Macedonio G., Gidaspow D., 2003. Multiparticle simulation of collapsing volcanic columns and pyroclastic flow. Journal of Geophysical Research, 108(B4), 2202.

Nodoushan E.J., Shakibaeinia A., Hosseini K., 2018. A multiphase meshfree particle method for continuum-based modeling of dry and submerged granular flows. Power Technology, 335, 258-274.

Pahar G., Dhar A., 2017. Coupled incompressible Smoothed Particle Hydrodynamics model for continuum-based modeling sediment transport. Advances in Water Resources, 102, 84-98.

Papanastasiou T.C., 1987. Flows of materials with yield. Journal of Rheology, 31(5), 385-404.

Ran Q., Tong J., Shao S., Fu X., Xu Y., 2015. Incompressible SPH scour model for movable bed dam break flows. Advances in Water Resources, 82, 39-50.

Ren B., Li C., Yan X., Lin M.C., Bonet J., Hu S.M., 2014. Multiple-fluid SPH simulation using a mixture model. ACM Transactions on Graphics, 33(5), 171.

Richardson J.F., Zaki W.N., 1954. Sedimentation and fluidization: Part I. Transactions of the Institution of Chemical Engineers, 32, 35-53.

Rondon L., Pouliquen O., Aussillous P., 2011. Granular collapse in a fluid: Role of the initial volume fraction. Physics of Fluids, 23, 073301.

Savage S.B., Babaei M.H., Dabros T., 2014. Modeling gravitational collapse of rectangular granular piles in air and water. Mechanics Research Communications, 56, 1-10.

Schiller L., Naumann Z., 1935. A drag coefficient correlation. V.D.I. Zeitung, 77, 318-320.

Shakibaeinia A., Jin Y.-C., 2011. A mesh-free particle model for simulation of mobile-bed dam break. Advances in Water Resources, 34(6), 794-807.

Shi H., Yu X., 2015. An effective Euler-Lagrange model for suspended sediment transport by open channel flows. International Journal of Sediment Research, 30, 361-370.

Shi H., Yu X., Dalrymple R.A., 2017. Development of a two-phase SPH model for sediment laden flows. Computer Physics Communications, 221, 259-272.

Si P., Shi H., Yu X., 2018. Development of a mathematical model for submarine granular flows. Physics of Fluids, 30, 083302.

Smagorinsky J., 1963. General circulation experiments with the primitive equations: I. the basic experiment. Monthly Weather Review, 91(3), 99-164.

Spinewine B., 2005. Two-layer flow behaviour and the effects of granular dilatancy in dam break induced sheet-flow. PhD thesis, Université catholique de Louvain.

Spinewine B., Capart H., 2013. Intense bed-load due to a sudden dam-break. Journal of Fluid Mechanics, 731, 579-614.

Trulsson M., Andreotti B., Claudin P., 2012. Transition from the viscous to inertial regime in dense suspensions. Physical Review Letters, 109, 118305.

Ulrich C., Leonardi M., Rung T., 2013. Multi-physics SPH simulation of complex marine-engineering hydrodynamic problems. Ocean Engineering, 64, 109-121.

Violeau D., Rogers B.D., 2016. Smoothed particle hydrodynamics (SPH) for free-surface flows: past, present and future. Journal of Hydraulic Research, 54(1), 1-26.

Wang C., Wang Y., Peng C., Meng X., 2016. Smoothed Particle Hydrodynamics simulation of water-soil mixture flows. Journal of Hydraulic Engineering, ASCE, 142(10), 04016032.

Wang C., Wang Y., Peng C., Meng X., 2017a. Two-fluid smoothed particle hydrodynamics simulation of submerged granular column collapse. Mechanics Research Communications, 79, 15-23.

Wang C., Wang Y., Peng C., Meng X., 2017b. Dilatancy and compaction effects on the submerged granular column collapse. Physics of Fluids, 29, 103307.

Wen C., Yu Y., 1966. Mechanics of fluidization. Chemical Engineering Progress Symposium

Series, 62(1), 100-111.

Wendland H., 1995. Piecewise pokynomial, positive definite and compactly supported radial functions of minimal degree. Advances in Computational Mathematics, 4(1), 389-396.

Wu W., Wang S.S.Y., 2007. One-dimensional modeling of dam-break flow over movable beds. Journal of Hydraulic Engineering, ASCE, 133(1), 48-58.

Yin X., Koch D., 2007. Hindered settling velocity and microstructure in suspensions of solid spheres with moderate Reynolds numbers. Physics of Fluids, 19, 093302.

Zubeldia E.H., Fourtakas G., Rogers B.D., Farias M.M., 2018. Multi-phase SPH model for simulation of erosion and scouring by means of the shields and Drucker-Prager criteria. Advances in Water Resources, 117, 98-114.

Figure Captions

Figure 1. Sketch of underwater granular column collapse in Wang et al. (2017b).

Figure 2. Particle configuration at t = 0 s after the gate removal in the loose-packing case. The red particles are those carrying the initial sediment volume fraction $\alpha_s = 0.53$ and represent the granular column.

Figure 3. Comparisons between numerical and experimental results of granular column profiles for the loose-packing case. Some results computed by the earlier two-phase SPH model of Shi et al. (2017) are also presented.

Figure 4. Comparisons between numerical and experimental results of granular column profiles for the dense-packing case. Some results computed by the earlier two-phase SPH model of Shi et al. (2017) are also presented.

Figure 5. Computed sequential configurations of free water surface and distributions of solid volume fraction carried by SPH particles for the loose-packing case. In (b), the region where solid grains are suspended is highlighted with an ellipse.

Figure 6. Computed sequential configurations of free water surface and distributions of solid volume fraction carried by SPH particles for the dense-packing case. In (b), the region where solid grains are suspended is highlighted with an ellipse.

Figure 7. Snapshot of the granular columns in the experiment at about t = 0.6 s. The figure is captured from the original video records of the collapse process on https://doi.org/10.1063/1.4986502.2. The arrows roughly represent the direction of the motion of the suspended solid particles in the front part of the granular flow. Top: the loose-packing case; bottom: the dense-packing case.

Figure 8. Fluid pressure of the SPH particles in the loose-packing case.

Figure 9. Fluid pressure of the SPH particles in the dense-packing case.

Figure 10. Distributions of the computed drag force in the loose-packing case at (a) t = 0.2 s and (b) t = 1.0 s, and the dense-packing case at (c) t = 0.3 s and (d) t = 2.4 s. The drag force on the solid particles $\mathbf{F}_\mathrm{d} = \gamma \alpha_s \left(\mathbf{u}_f - \mathbf{u}_s \right)$, and its norm $\left| \mathbf{F}_\mathrm{d} \right|$ is normalized by $\rho_s g$.

Figure 11. Comparisons of the simulated sequential profiles of the granular columns with and without the drag force for (a) the loose-packing case and (b) the dense-packing case.

Figure 12. Evolution of the water vortex induced by the collapse of the loosely packed

granular column.

Figure 13. Evolution of the water vortex induced by the collapse of the densely packed granular column.

Figure 14. Set-up of the dam-break erosion experiment of Spinewine (2005).

Figure 15. Comparisons between the computed and the measured interfaces separating the clear water layer, the moving bed layer with intense sediment transport, and the static sediment bed ~~profiles of the free water surface and the movable bed~~ at (a) t = 0.25 s, (b) t = 0.50 s, (c) t = 0.75 s, (d) t = 1.00 s, (e) t = 1.25 s, and (f) t = 1.50 s. The “water” in the legend is for the free water surface, while the “moving bed” and the “static bed” represent the top of the moving bed layer and that of the motionless sediment bed, respectively.

Figure 16. Comparisons between numerical (red solid lines) and experimental (black dots) profiles of longitudinal velocity at (a) t = 0.60 s, (b) t = 1.00 s, and (c) t = 1.40 s in the flat bed case. The black lines are the computed profiles of the free water surface (solid lines), the top of the moving bed layer (long dashes), and the top of the static bed (short dashes).

Figure 17. Simulated (a) particle configuration and sediment concentration, and (b) pressure field at t = 0.15 s. The dotted line in (b) is obtained according to the particle configuration in (a) and represents the bed surface.

Figure 18. Computed distributions of (a) water velocity in the fluid column and in the granular material, (b) sediment velocity inside the granular bed, and (c) drag force on the solid phase at t = 0.15 s. The red dashed lines represent the surface of the moving bed. The marked region in (b) is where the magnitude of the dynamic pressure force $\left|-\alpha_s \nabla p_f^{\mathrm{d}}\right| = \left|-\alpha_s \nabla p_f + \alpha_s \rho_s \mathbf{g}\right|$ is larger than $0.6\rho_s g$. The contour plot in (c) is for the ratio of the magnitude of the drag force $\left|\mathbf{F}_{\mathrm{d}}\right|$ to that of the dynamic pressure force. The contour line of $\left|\mathbf{F}_{\mathrm{d}}\right| \Big/ \left|-\alpha_s \nabla p_f^{\mathrm{d}}\right| = 1$ is drawn in (c).

Figure 19. (a) Particle configuration and sediment concentration, and (b) pressure field at t = 0.70 s. The high-pressure region due to the wave impact at the leading edge of the dam-break flow is highlighted in (b).

Figure 20. Same as Figure 18 but for the results at t = 0.70 s.

Figure 21. (a) Particle configuration and sediment concentration, and (b) pressure field at t =

1.50 s.

Figure 22. Same as Figure 18 but for the results at t = 1.50 s.

Table Captions

Table 1. Model parameters used in this study.

Table 2. Analysis on the sensitivities of granular avalanche front position and column height in underwater granular column collapse and flow leading position in dam-break erosion to model parameters in the constitutive law for sediment phase.

Table 3. Comparisons between numerical and experimental results of dam-break flow leading position and maximum bed height at typical instants of time.

Table 1. Model parameters used in this study

Cases	C_f	C_s	n	α_{sm}	c_1	c_2	α_{s0}	K	α_*	α^*	χ	μ_2	$\sqrt{I_0}$
Underwater granular column collapse	0.1	0.1	5	0.60	1.0	0.1	0.60	3×10^4 Pa	0.45	0.62	1.5	0.85	0.1
Sediment transport by dam-break flows	0.1	0.1	5	0.58	1.0	0.5	0.58	10^5 Pa	0.48	0.58	2.5	0.82	0.1

Table 2. Analysis on the sensitivities of granular avalanche front position and column height in underwater granular column collapse and flow leading position in dam-break erosion to model parameters in the constitutive law for sediment phase.

Varying parameters	Varying ranges	Underwater granular column collapse		Sediment transport by dam-break flows
		Front position L at t = 0.5 s in the loose-packing case (cm)	Column height H at t = 4.0 s in the dense-packing case (cm)	Flow leading position at t = 0.50 s (m)
μ_2	$\tan\phi \sim 1.0$	12.1 ~ 11.7	7.0 ~ 7.2	1.16 ~ 1.03
I_0	0.01 ~ 0.09	11.8 ~ 12.0	7.2 ~ 7.0	1.09 ~ 1.11
c_1	0.75 ~ 1.00	11.6 ~ 11.8	7.1 ~ 7.2	1.12 ~ 1.09
c_2	0.01 ~ 1.00	11.9 ~ 11.6	7.1 ~ 7.3	1.14 ~ 1.03
K	$10^4 \sim 10^9$	11.1 ~ 15.3	7.4 ~ 5.6	1.01 ~ 1.09
χ	1.5 ~ 5.5	11.8 ~ 10.5	7.1 ~ 7.7	1.03 ~ 1.14

Table 3. Comparisons between numerical and experimental results of dam-break flow leading position and maximum bed height at typical instants of time.

	Leading position of dam-break flow (m)		Maximum bed height (cm)	
	Exp.	Comp.	Exp.	Comp.
t = 0.25 s	0.56	0.69	5.7	7.4
t = 0.50 s	1.16	1.15	8.2	8.0
t = 0.75 s	1.74	1.75	11.6	8.9
t = 1.00 s	2.17	2.15	8.2	7.8
t = 1.25 s	2.54	2.54	7.4	6.1
t = 1.50 s	2.93	2.98	5.5	6.4

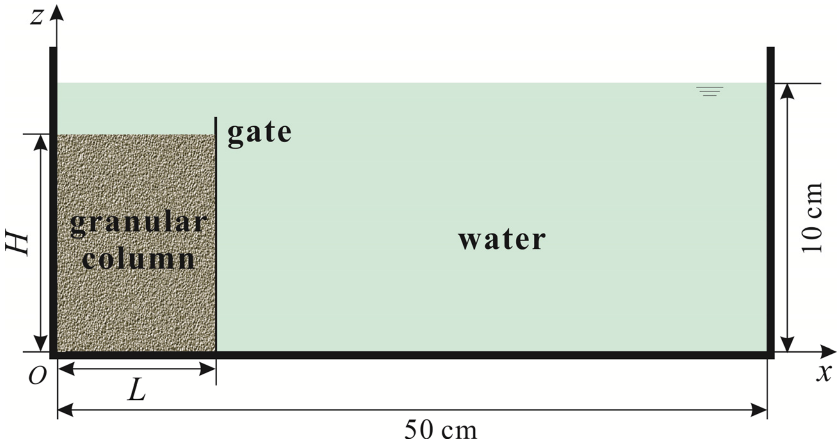

Figure 1. Sketch of underwater granular column collapse in Wang et al. (2017b).

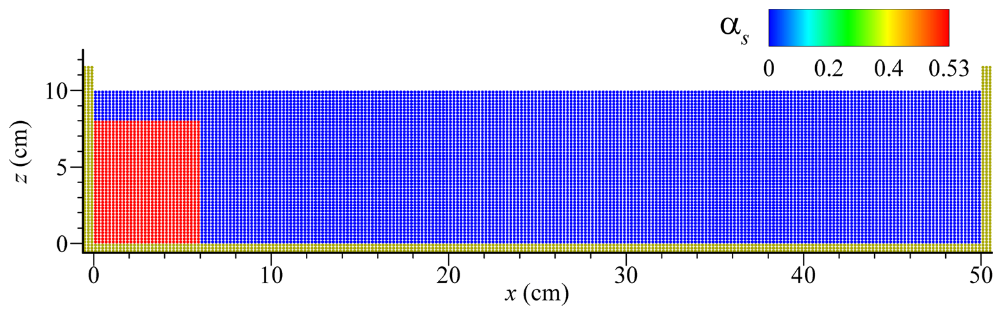

Figure 2. Particle configuration at t = 0 s after the gate removal in the loose-packing case. The red particles are those carrying the initial sediment volume fraction $\alpha_s = 0.53$ and represent the granular column.

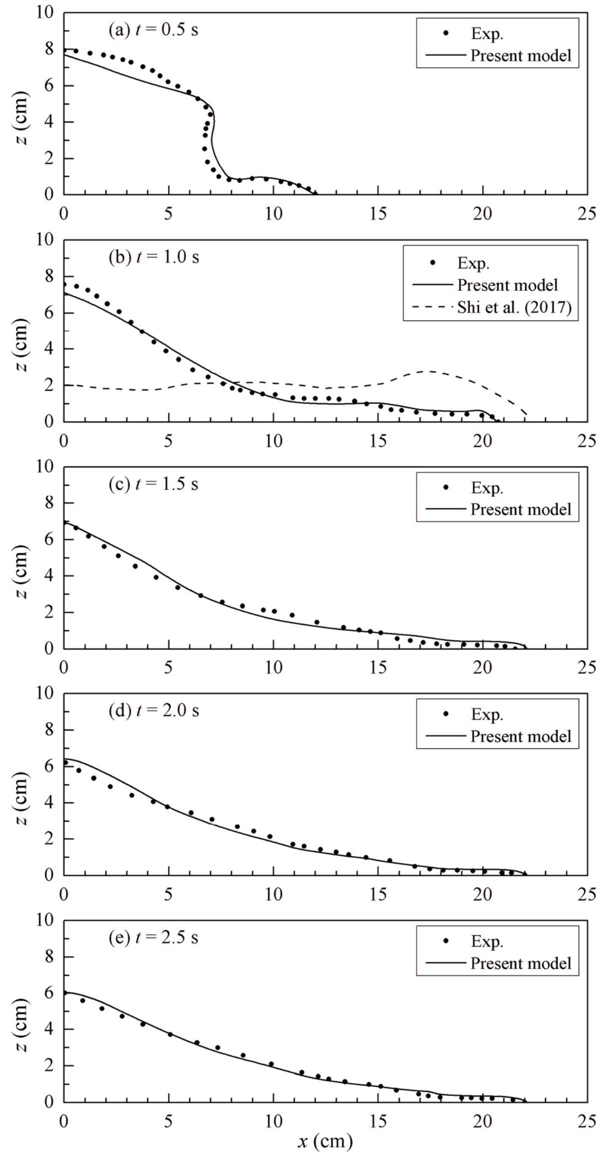

Figure 3. Comparisons between numerical and experimental results of granular column profiles for the loose-packing case. Some results computed by the earlier two-phase SPH model of Shi et al. (2017) are also presented.

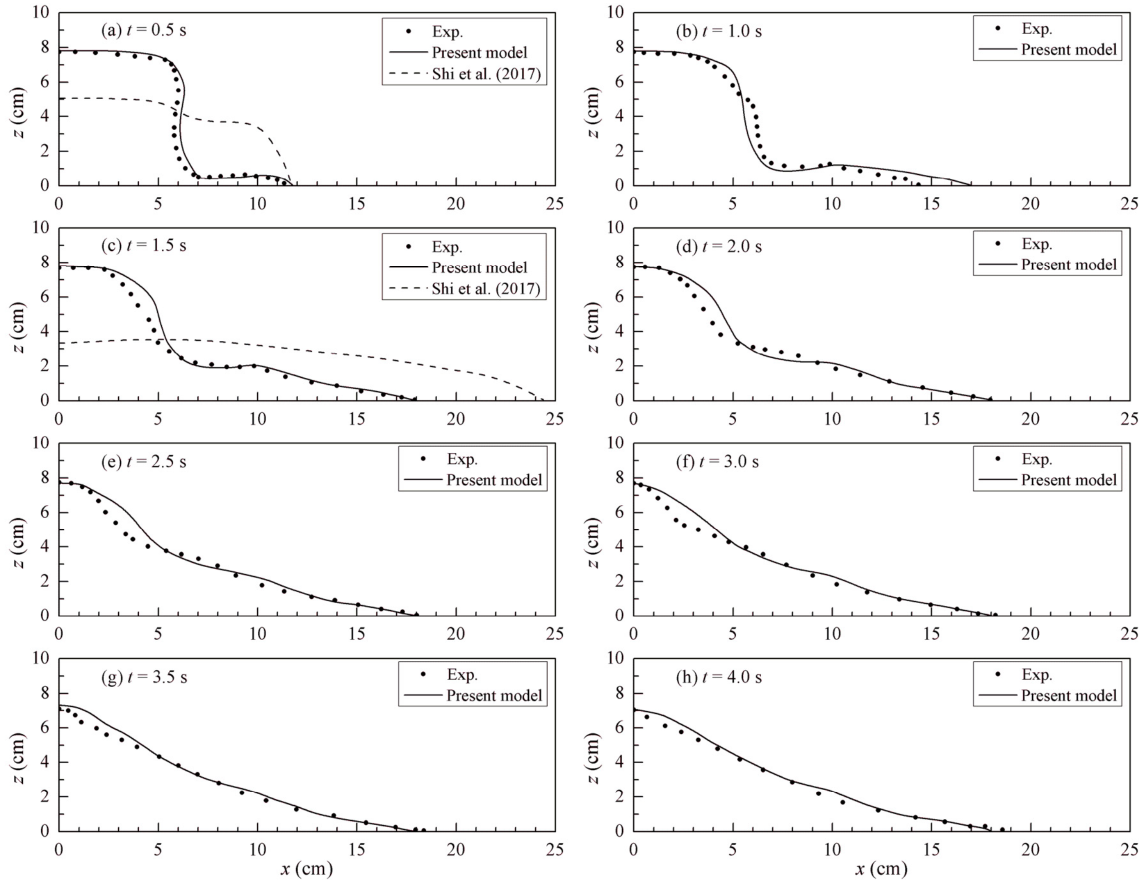

Figure 4. Comparisons between numerical and experimental results of granular column profiles for the dense-packing case. Some results computed by the earlier two-phase SPH model of Shi et al. (2010) are also presented.

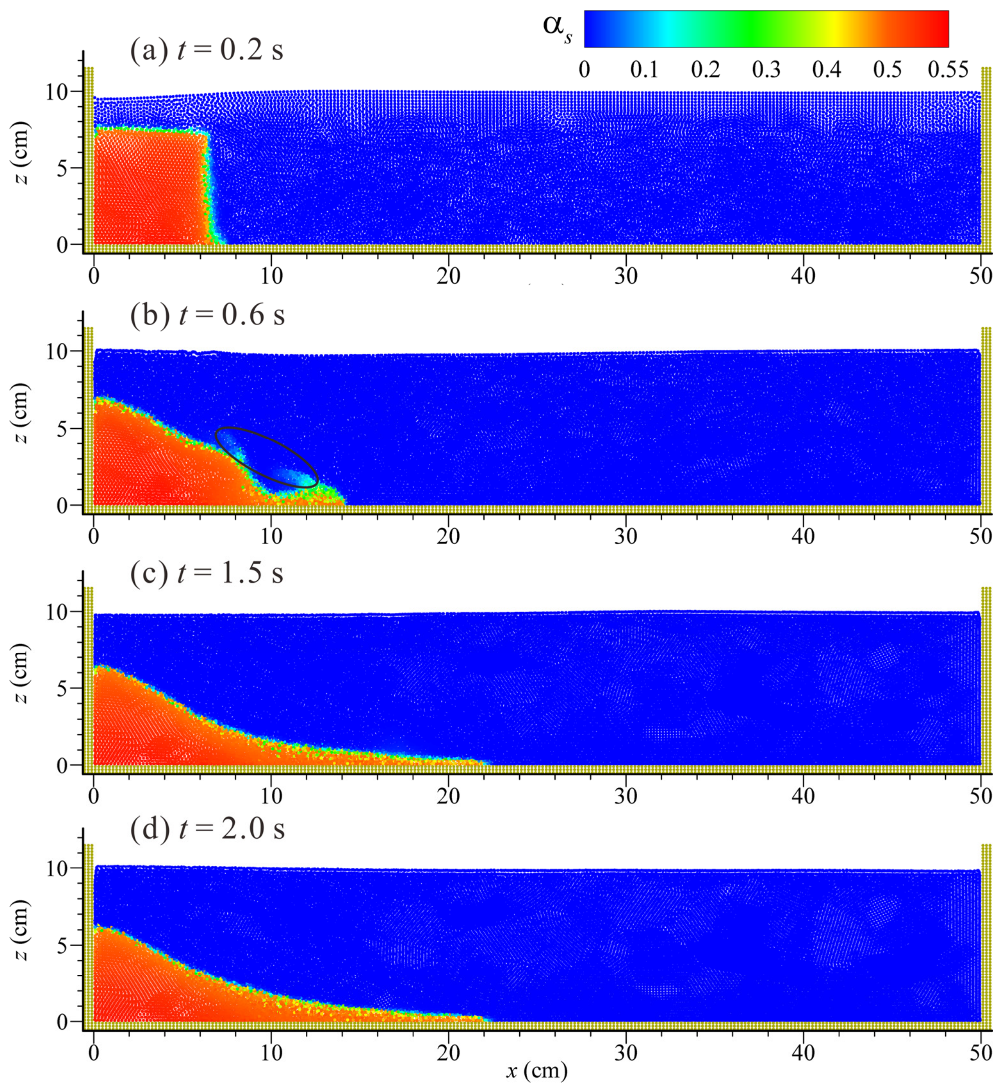

Figure 5. Computed sequential configurations of free water surface and distributions of solid volume fraction carried by SPH particles for the loose-packing case. In (b), the region where solid grains are suspended is highlighted with an ellipse.

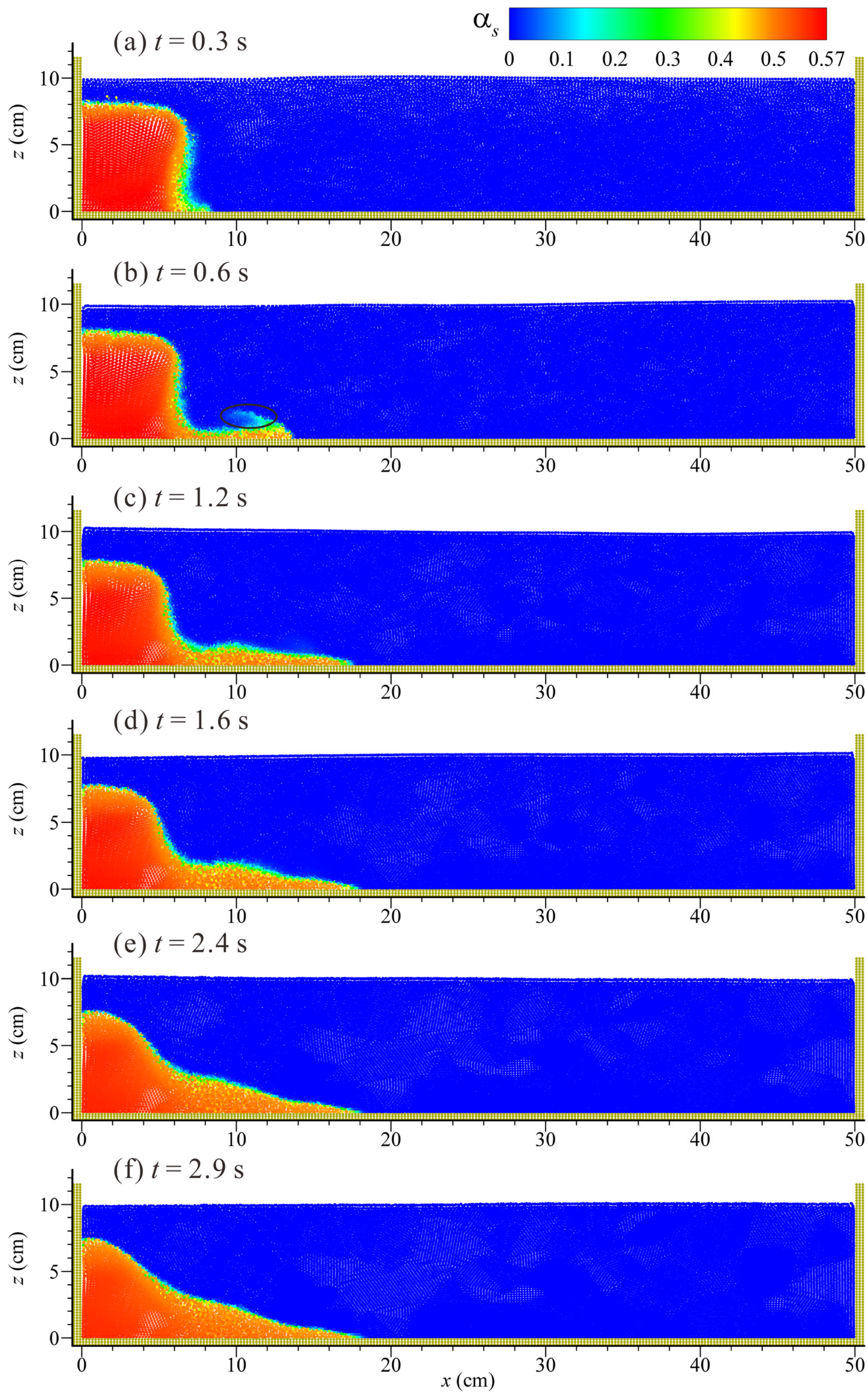

Figure 6. Computed sequential configurations of free water surface and distributions of solid volume fraction carried by SPH particles for the dense-packing case. In (b), the region where solid grains are suspended is highlighted with an ellipse.

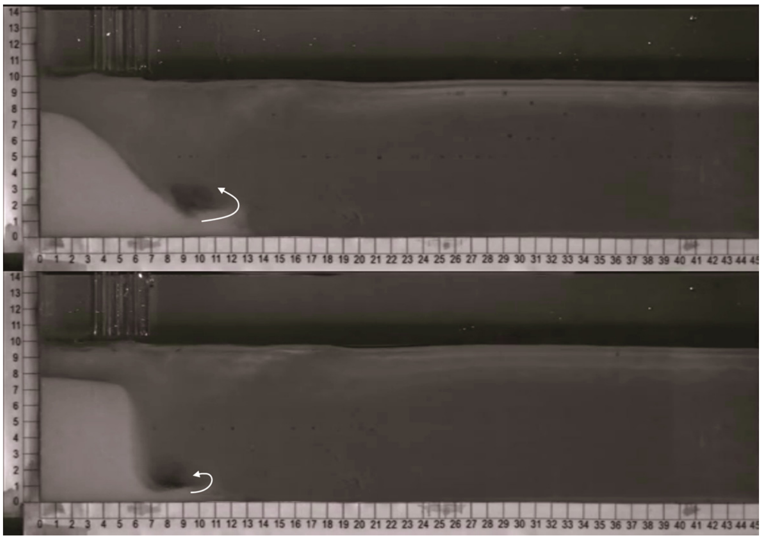

Figure 7. Snapshot of the granular columns in the experiment at about t = 0.6 s. The figure is captured from the original video records of the collapse process on https://doi.org/10.1063/1.4986502.2. The arrows roughly represent the direction of the motion of the suspended solid particles in the front part of the granular flow. Top: the loose-packing case; bottom: the dense-packing case.

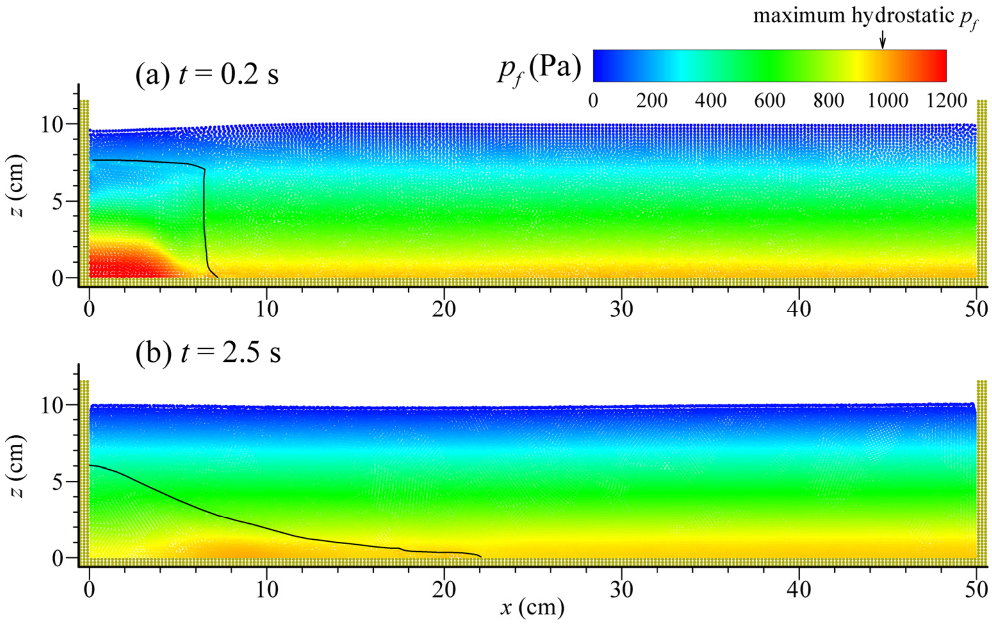

Figure 8. Fluid pressure of the SPH particles in the loose-packing case.

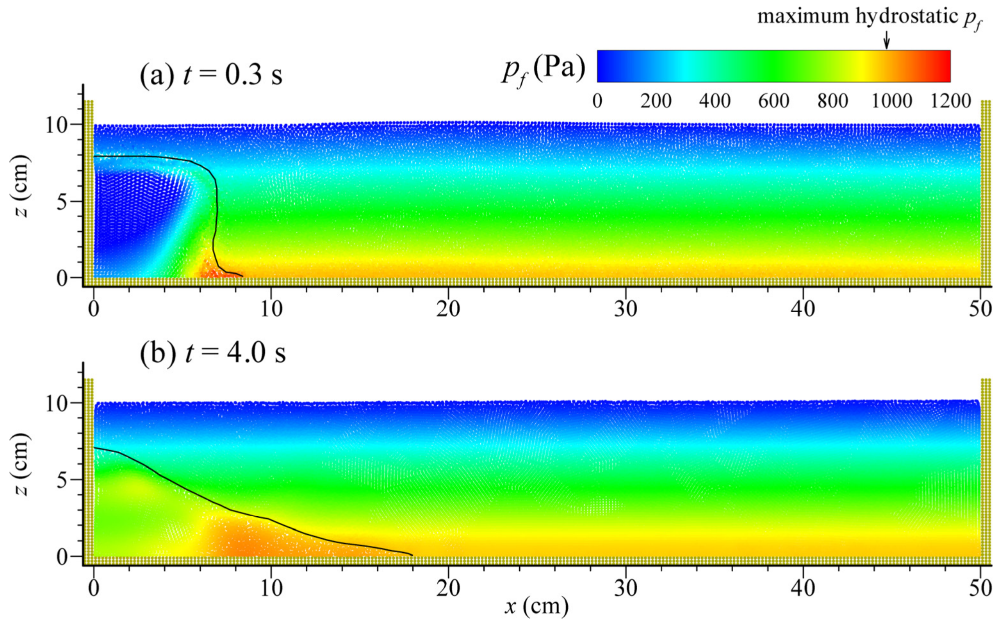

Figure 9. Fluid pressure of the SPH particles in the dense-packing case.

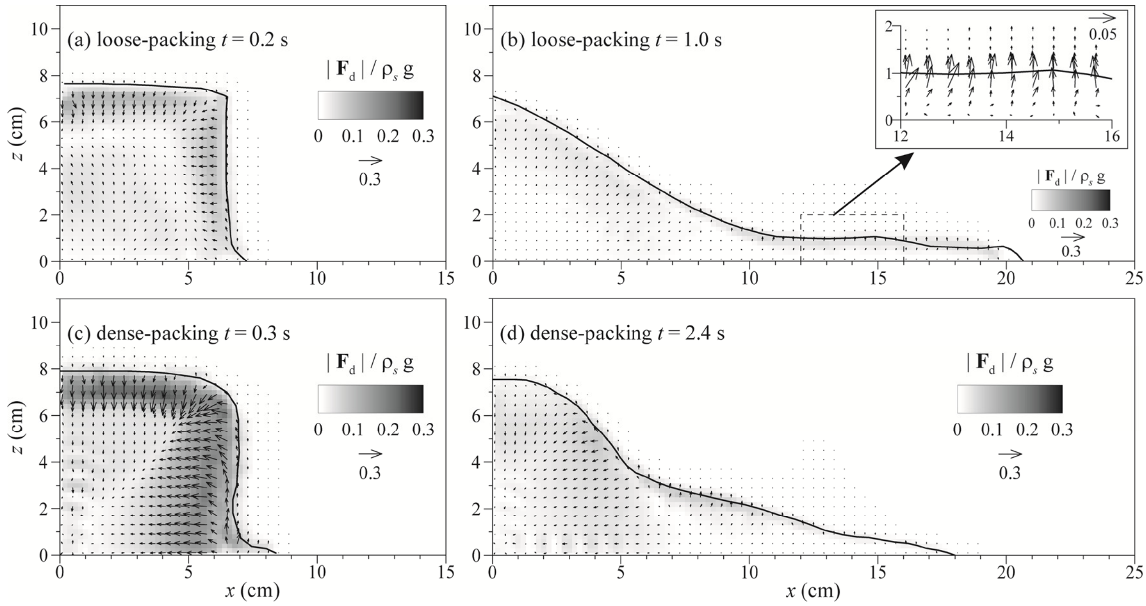

Figure 10. Distributions of the computed drag force in the loose-packing case at (a) t = 0.2 s and (b) t = 1.0 s, and the dense-packing case at (c) t = 0.3 s and (d) t = 2.4 s. The drag force on the solid particles $\mathbf{F}_\mathrm{d} = \gamma\alpha_s\left(\mathbf{u}_f - \mathbf{u}_s\right)$, and its norm $\left|\mathbf{F}_\mathrm{d}\right|$ is normalized by $\rho_s g$.

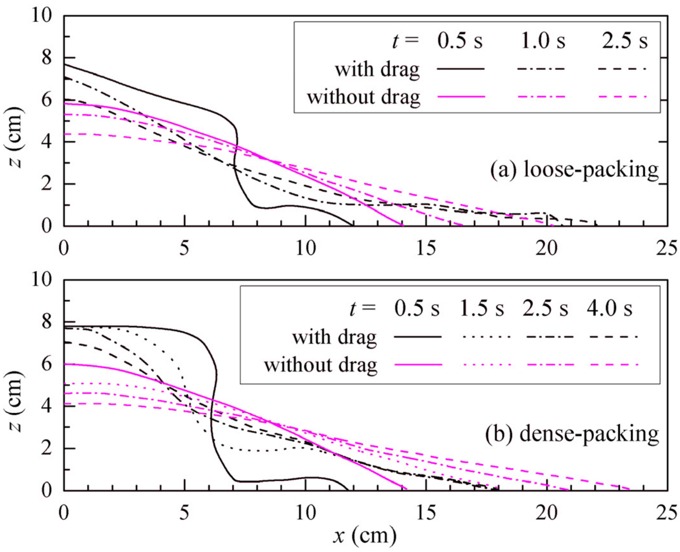

Figure 11. Comparisons of the simulated sequential profiles of the granular columns with and without the drag force for (a) the loose-packing case and (b) the dense-packing case.

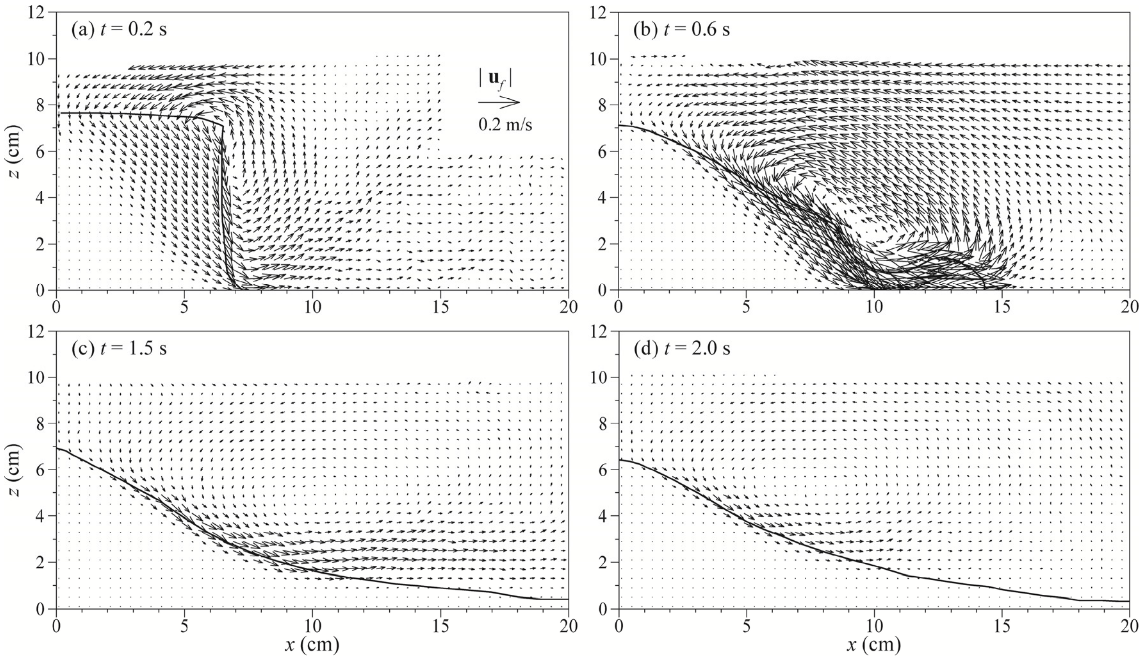

Figure 12. Evolution of the water vortex induced by the collapse of the loosely packed granular column.

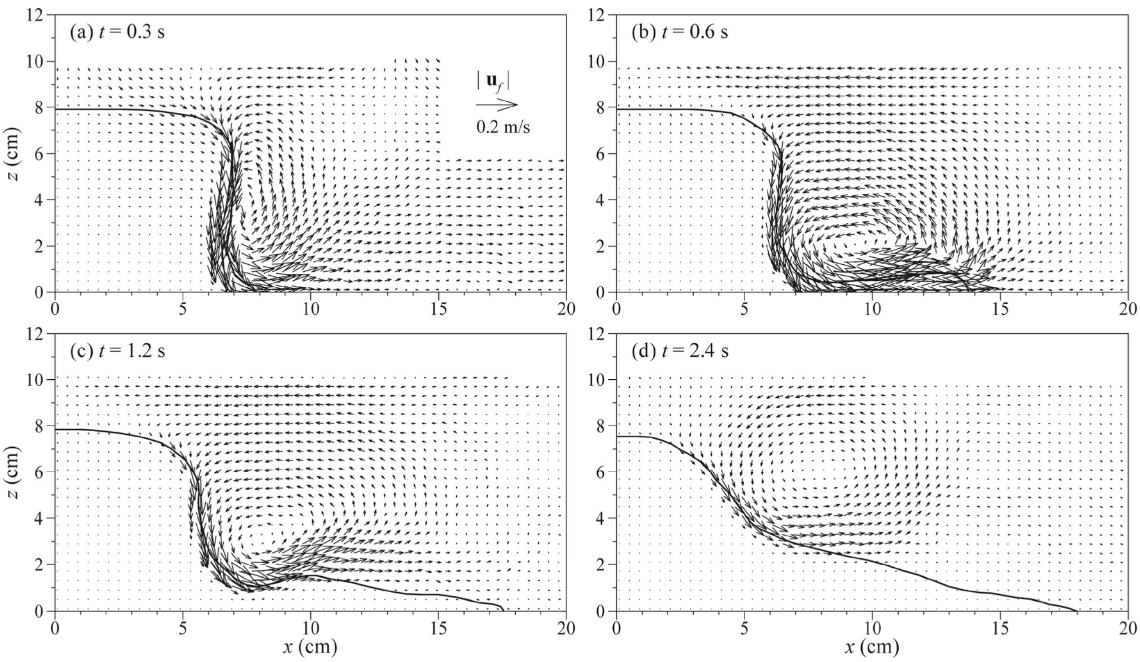

Figure 13. Evolution of the water vortex induced by the collapse of the densely packed granular column.

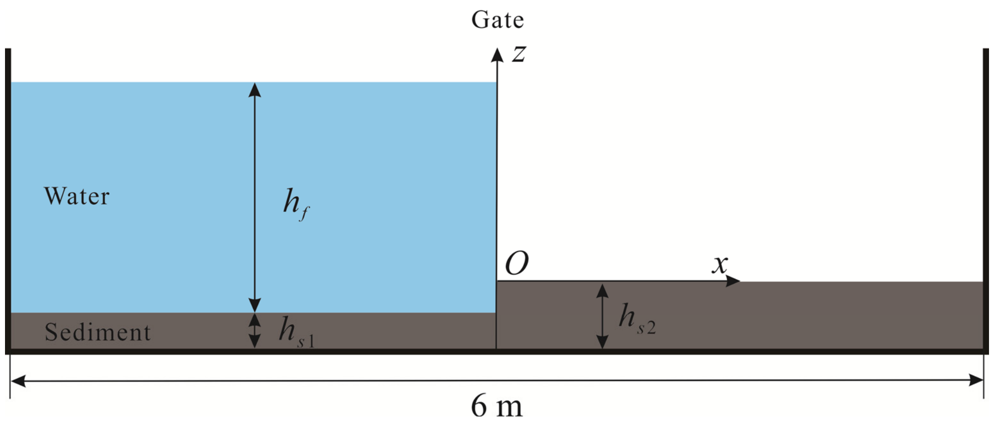

Figure 14. Set-up of the dam-break erosion experiment of Spinewine (2005).

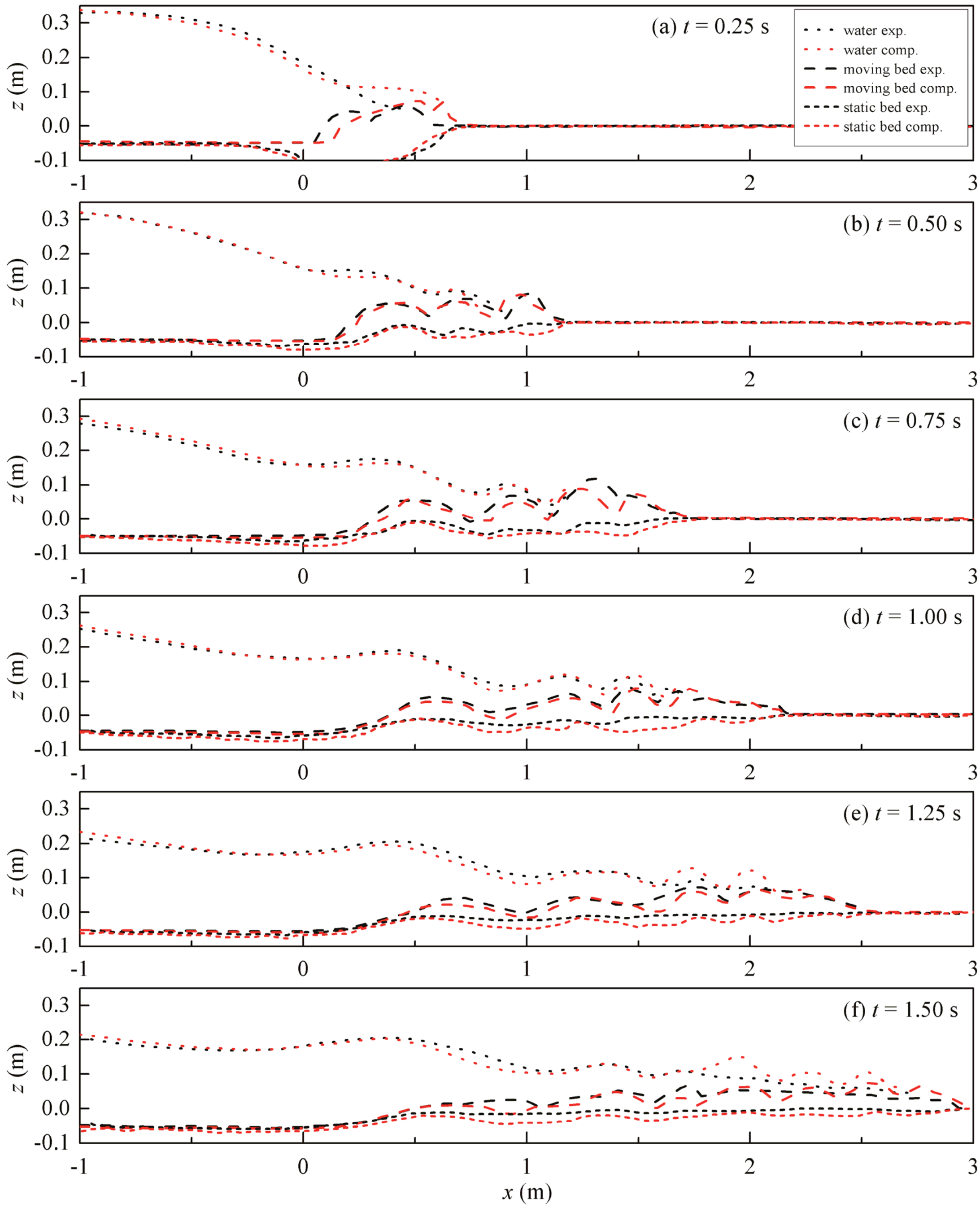

Figure 15. Comparisons between the computed and the measured interfaces separating the clear water layer, the moving bed layer with intense sediment transport, and the static sediment bed ~~profiles of the free water surface and the movable bed~~ at (a) $t = 0.25$ s, (b) $t = 0.50$ s, (c) $t = 0.75$ s, (d) $t = 1.00$ s, (e) $t = 1.25$ s, and (f) $t = 1.50$ s. The "water" in the legend is for the free water surface, while the "moving bed" and the "static bed" represent the top of the moving bed layer and the motionless sediment bed, respectively.

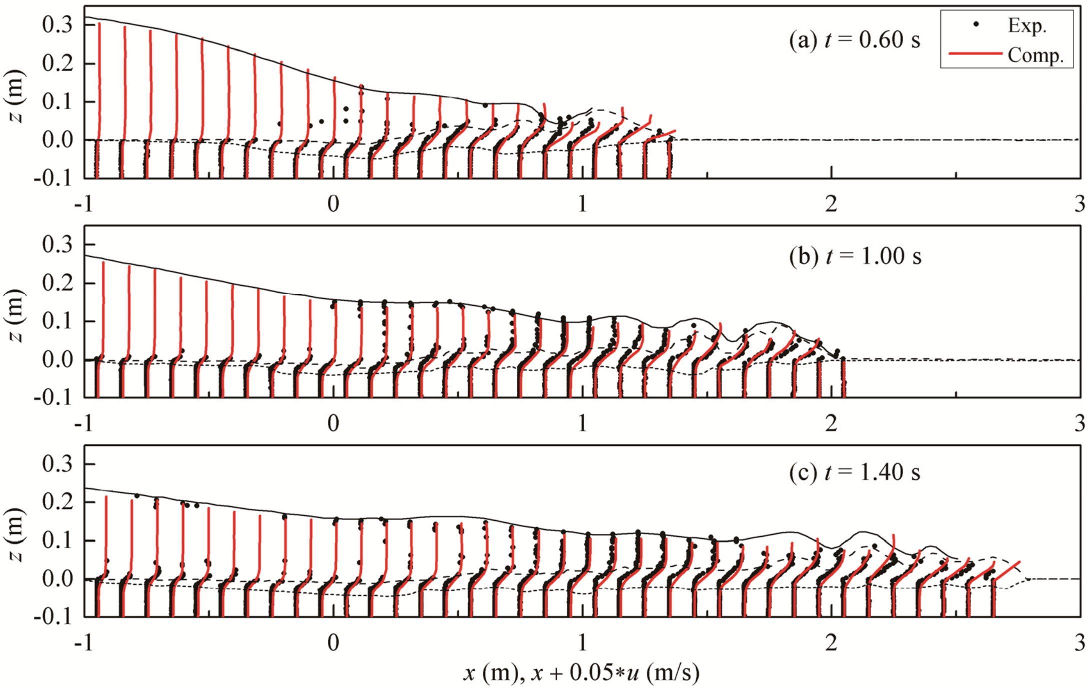

1053

1054 Figure 16. Comparisons between numerical (red solid lines) and experimental (black dots)
1055 profiles of longitudinal velocity at (a) t = 0.60 s, (b) t = 1.00 s, and (c) t = 1.40 s in the flat bed
1056 case. The black lines are the computed profiles of the free water surface (solid lines), the top
1057 of the moving bed layer (long dashes), and the top of the static bed (short dashes).
1058

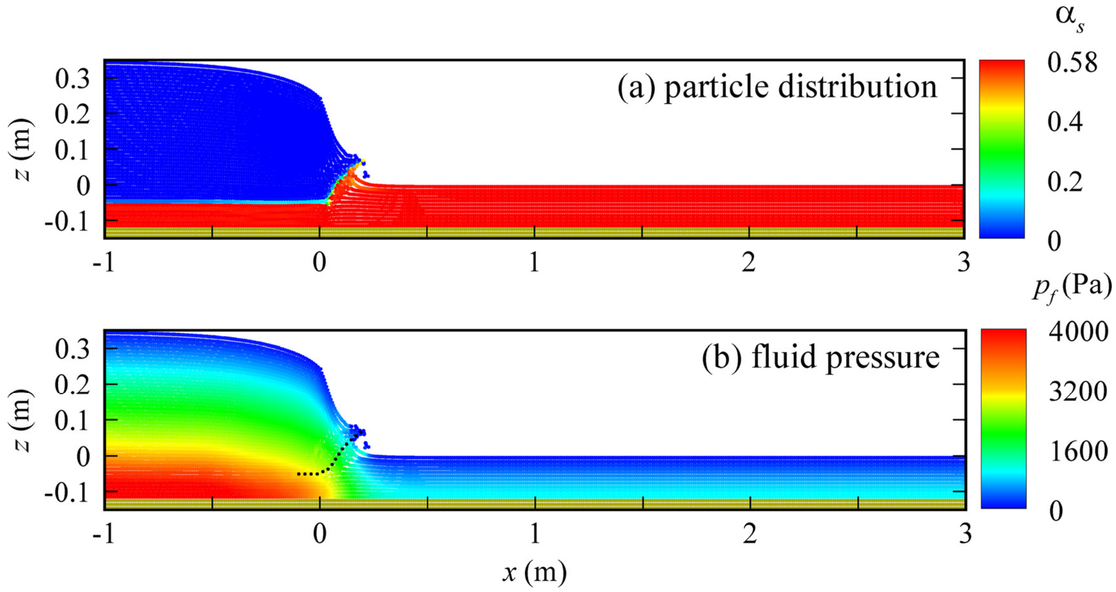

Figure 17. Simulated (a) particle configuration and sediment concentration, and (b) pressure field at t = 0.15 s. The dotted line in (b) is obtained according to the particle configuration in (a) and represents the bed surface.

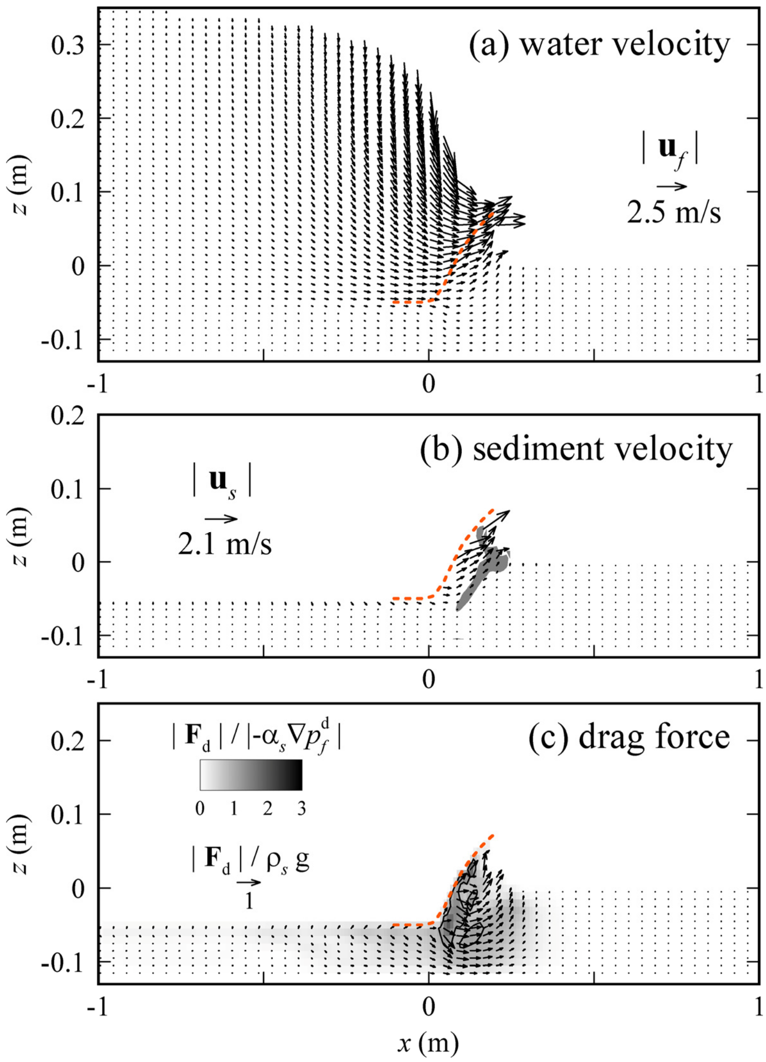

Figure 18. Computed distributions of (a) water velocity in the fluid column and in the granular material, (b) sediment velocity inside the granular bed, and (c) drag force on the solid phase at $t = 0.15$ s. The red dashed lines represent the surface of the moving bed. The marked region in (b) is where the magnitude of the dynamic pressure force $\left|-\alpha_s \nabla p_f^{\mathrm{d}}\right| = \left|-\alpha_s \nabla p_f + \alpha_s \rho_s \mathbf{g}\right|$ is larger than $0.6\rho_s g$. The contour plot in (c) is for the ratio of the magnitude of the drag force $\left|\mathbf{F}_\mathrm{d}\right|$ to that of the dynamic pressure force. The contour line of $\left|\mathbf{F}_\mathrm{d}\right| / \left|-\alpha_s \nabla p_f^{\mathrm{d}}\right| = 1$ is drawn in (c).

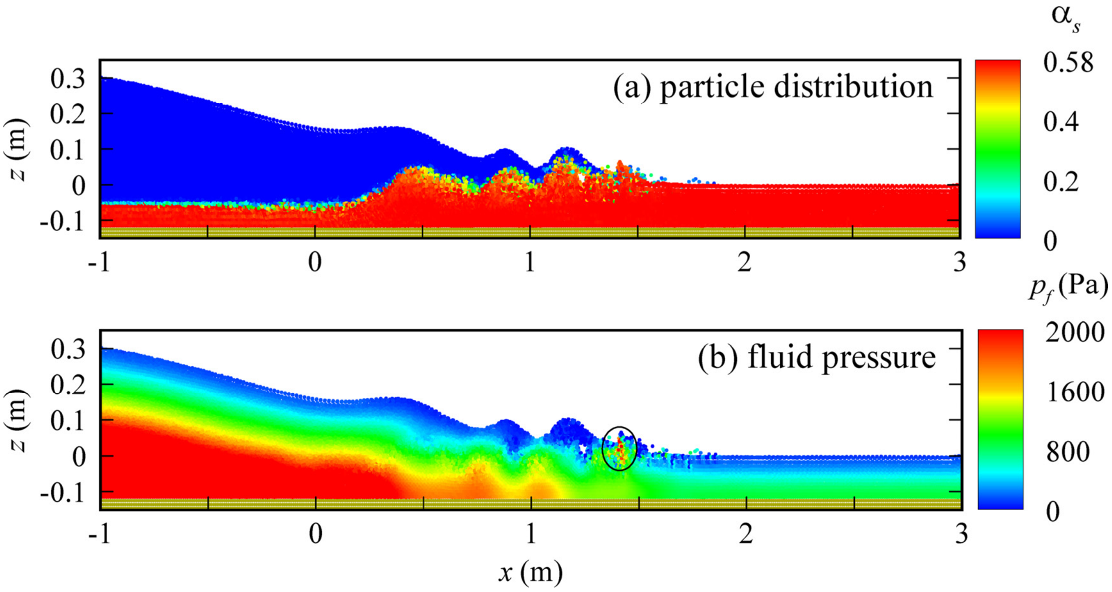

Figure 19. (a) Particle configuration and sediment concentration, and (b) pressure field at t = 0.70 s. The high-pressure region due to the wave impact at the leading edge of the dam-break flow is highlighted in (b).

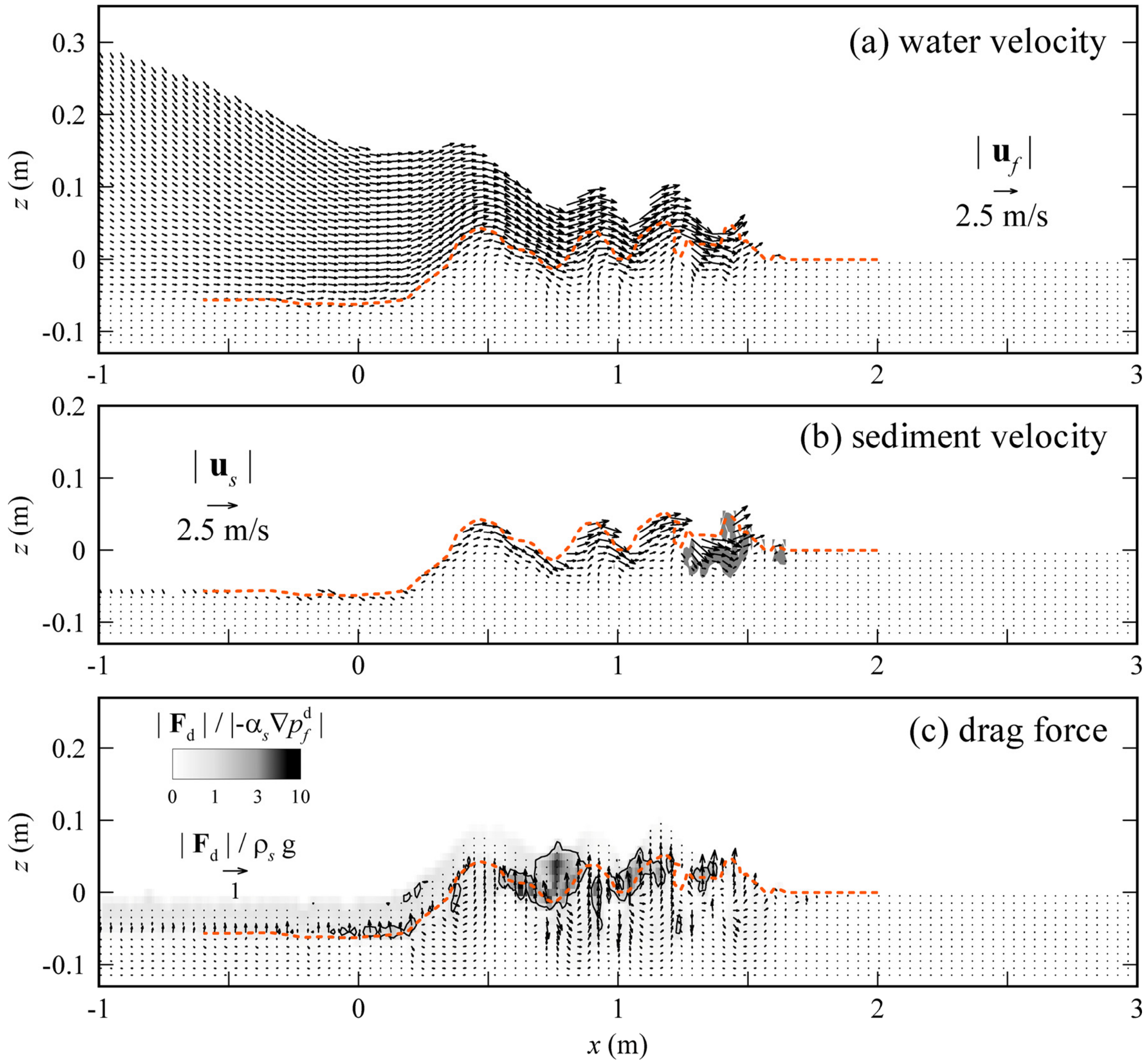

Figure 20. Same as Figure 18 but for the results at t = 0.70 s.

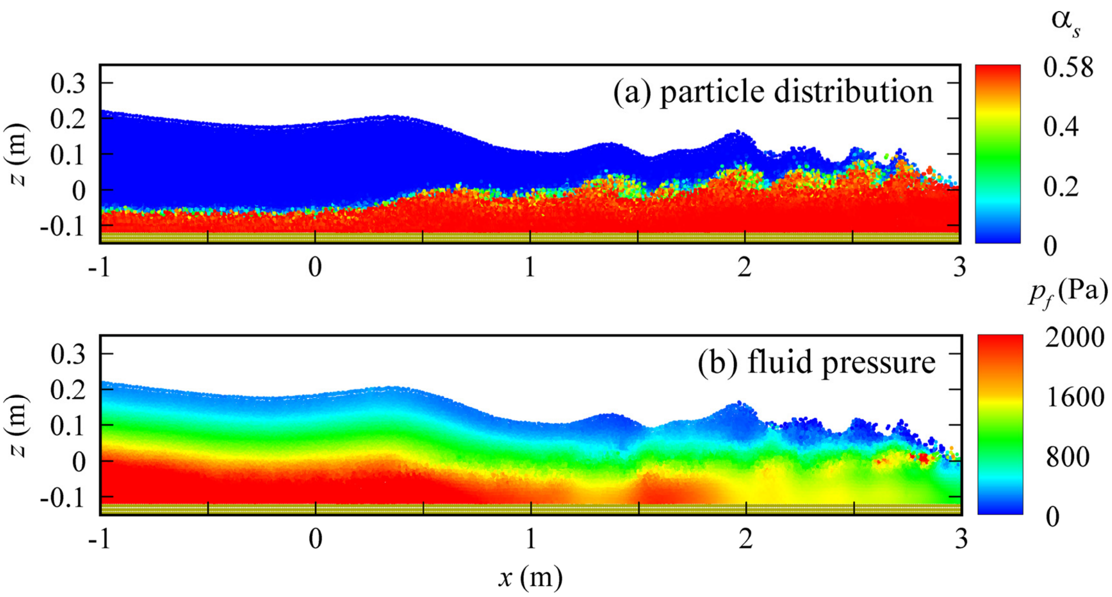

Figure 21. (a) Particle configuration and sediment concentration, and (b) pressure field at t = 1.50 s.

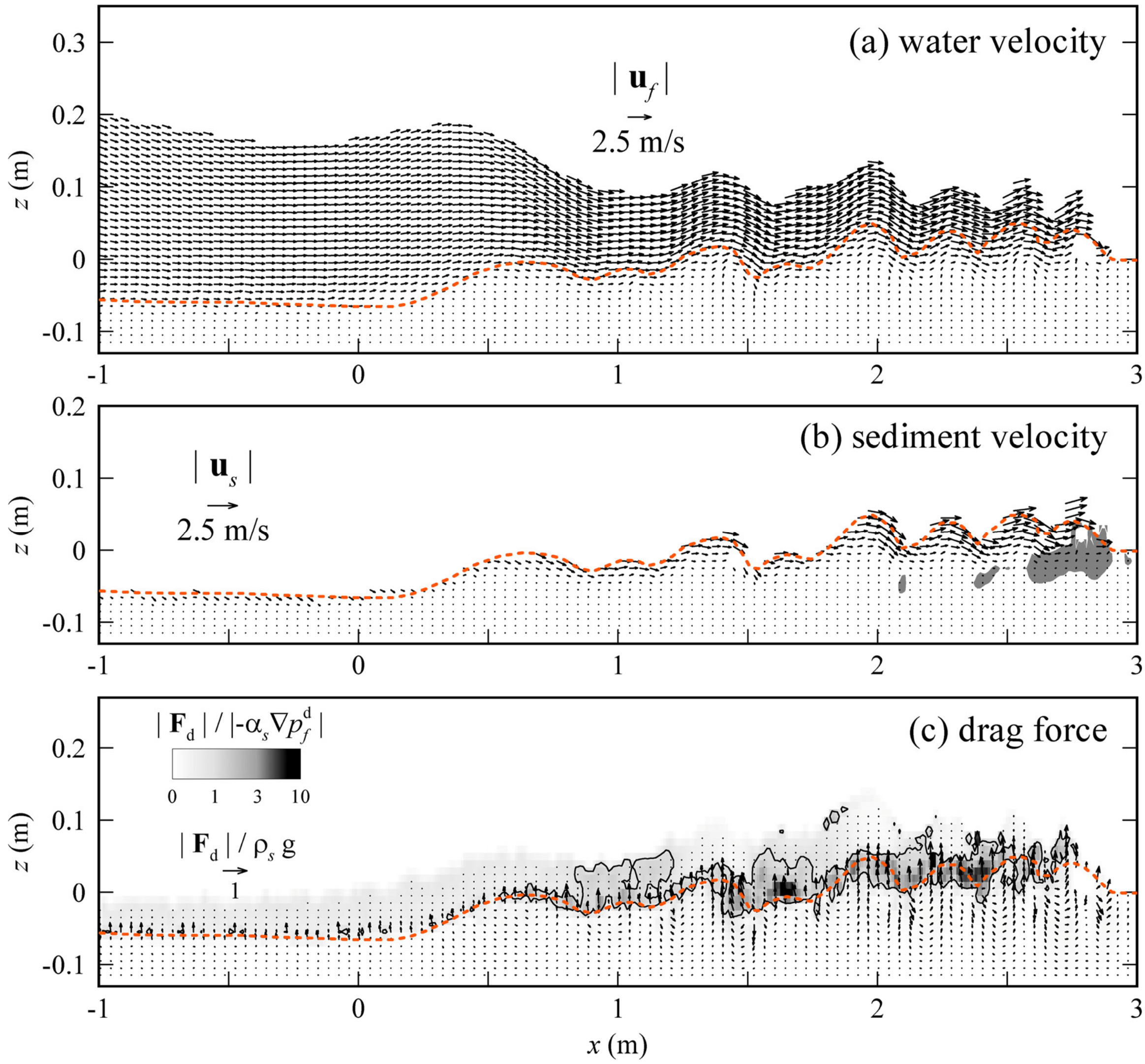

1085

1086 Figure 22. Same as Figure 18 but for the results at t = 1.50 s.